Geoscientific
Model Development
Discussions

An evaluation of the regional distribution and wet deposition of secondary inorganic aerosols and their gaseous precursors in IFS-COMPO cycle 49R1

Jason E. Williams[1], Swen Metzger[2], Samuel Rémy[3], Vincent Huijnen[1] and Johannes Flemming[4]

1 R&D Weather and Climate Modeling, Royal Netherlands Meteorological Institute, De Bilt, the Netherlands

2 ResearchConcepts Io GmbH, Freiburg, Germany

3 HYGEOS, Lille, France

4 European Centre for Medium-Range Weather Forecasts, Bonn, Germany

Correspondence to : Jason Williams (jason.williams@knmi.nl)

Abstract

Secondary Inorganic Aerosol (SIA) constitutes a considerable fraction of total particulate matter exposure, making it an important component of any atmospheric composition and air quality forecasting system. The subsequent loss of SIA to the surface, via both dry and wet deposition, determines the exposure time for humans and the extent of damage imposed on sensitive ecosystems due to increased surface acidity. This study provides a description and evaluation of recent updates to aerosol production, scavenging, and wet deposition processes in the global IFS-COMPO chemical forecasting system, used within the Copernicus Atmosphere Monitoring Service. The implementation of the EQSAM4Clim simplified thermodynamic module in IFS-COMPO cycle 49R1 alters the phase transfer efficiency of SIA precursor gases (sulphur dioxide, nitric acid, and ammonia), which significantly affects particulate SIA concentrations by modifying the fraction converted into aerosol form. Comparisons with surface observational data from Europe, the U.S., and Southeast Asia during 2018 indicate reductions in the global annual mean bias for both sulphates and nitrates. Updating the IFS-COMPO model to cycle 49R1 increases the burden and lifetime of sulphate and ammonium particles by one-third. Coupling EQSAM4Clim with IFS-COMPO improves the representation of ammonia-ammonium partitioning across regions, while the effect on sulphate is minimal. For nitric acid and nitrates, the phase partitioning is also significantly altered, with lower particulate concentrations leading to an excess of gas-phase nitric acid and an associated improvement in surface nitrate predictions. The impact on total regional wet deposition is generally positive, although sulphates in the U.S. and ammonium particles in Southeast Asia are strongly influenced by precursor emission estimates. Overall, these results provide confidence in the ability of IFS-COMPO cycle 49R1 to deliver accurate global-scale deposition fluxes of sulphur and nitrogen.

1. Introduction

Secondary Inorganic Aerosols (SIA) are found throughout the troposphere, where their concentrations depend on temperature (T), relative humidity (RH), and the concentrations of inorganic precursor gases, namely water vapor (H_2O), sulfur dioxide (SO_2), ammonia (NH_3), and nitric acid (HNO_3). High concentrations of SIA contribute to total particulate matter, accumulating in size bins of 1.0 µm ($PM_{1.0}$), 2.5 µm ($PM_{2.5}$), and 10 µm (PM_{10}) (Liu et al., 2022), and have detrimental effects on both human health and visibility (Sharma et al., 2020; Ting et al., 2021). The main types of SIA are ammonium sulfate (($NH_4)_2SO_4$), ammonium bisulfate (NH_4HSO_4), and ammonium nitrate (NH_4NO_3). Once formed, sulfates are very stable and deposit to the surface, while NH_4NO_3 is more unstable and can decompose back into precursor gases (Feick and Hainer, 1954), depending on T and RH. These particles can be transported out of source regions, influencing air quality in neighboring countries (e.g., Vieno et al., 2014; Chang et al., 2022). Anthropogenic activity significantly contributes to SIA formation through the emission of NO_x (oxidized nitrogen in the form of NO and NO_2), NH_x (reduced nitrogen), and SO_2. There has been a general trend of decreasing sulfur (S) and nitrogen (N) emissions in the EU, U.S., and China (Tørseth et al., 2012; Aas et al., 2019; Benish et al., 2022; Jiang et al., 2022), leading to an increasing fraction of SIA being NH_4NO_3. This results in a decrease in the lifetime of SIA due to the increased meteorological instability of NH_4NO_3 (e.g., Williams et al., 2015; Metzger et al., 2002, 2006), reducing the potential for long-range transport out of source regions (He et al., 2018).

At RH values above 50%, most SIA aggregates water and exists in a deliquescent state. At high RH, SIA formation is enhanced (Gao et al., 2020); therefore, under constant or changing emissions, SIA is likely to become more ubiquitous in a warming atmosphere. The hygroscopic growth of SIA alters its optical properties (scattering and absorption) and interactions with gas-phase trace species via changes in pH (e.g., Jayne et al., 1990; Shi et al., 2018). The concentrated salt solution produced typically has higher ionic strength than cloud droplets, with pH values ranging from -1 to 6 (Ault, 2020). The high solubility of SIA leads to scavenging into aqueous aerosols and clouds, which is a dominant loss mechanism. This has implications for the acidification of sensitive ecosystems and increased eutrophication due to high nitrogen loading in inland water bodies, potentially exceeding critical loads for vegetation (e.g., Sun et al., 2020). Nitrogen loading also enhances carbon uptake by land (Holland et al., 1997; Reary et al., 2008). Once dissolved in solution, SIA dissociates efficiently into its ionic constituents (e.g., nitrate (NO_3^-), ammonium (NH_4^+), and sulfate (SO_4^{2-})), which are then deposited on land during precipitation events.

There are distinct differences in the primary source terms for various SIA species. For NO_x and NH_x species, particle formation is sensitive to resident gas-phase precursors, temperature, and RH in the absence of aqueous-phase droplets. For SO_4^{2-}, production occurs almost exclusively in the aqueous phase after SO_2 is scavenged into clouds and fog, with cumulative oxidation rates dependent on the prescribed pH in solution. Recent studies highlight the importance of accurately representing cloud pH for determining long-term trends in SO_4^{2-} production (Thurock et al., 2019; Myriokefalitakis et al., 2022). The representation of acidity in tropospheric aerosols and clouds varies significantly across large-scale atmospheric models. The simplest approach is to assume a fixed cloud water pH between 5.0 and 5.6, effectively representing the impact of dissolved CO_2. A more accurate approach incorporates the influence of other dissolved species that either acidify (e.g., HNO_3, H_2SO_4) or buffer (e.g., NH_3) solution pH once scavenged through irreversible uptake. This is the method adopted in the Integrated Forecasting System with atmospheric composition extension (IFS-COMPO) for both cloud and precipitation. Other SO_4^{2-} production mechanisms involving compounds such as methyl hydroperoxide (CH_3OOH) are of secondary importance (Myriokefalitakis et al., 2022). More buffering by NH_3 accelerates conversion rates, as the reaction of HSO_3^- is slower than that of SO_3^{2-} (Warneck, 1991).

A major loss mechanism for SIA is wet deposition through precipitation. Previous global tropospheric modeling studies have focused on the temporal accuracy and annual deposition totals at continental scales for NH_x and SO_x (Zhang et al., 2012; Kanikadou et al., 2016; Ge et al., 2021). Multi-model intercomparison studies have also examined variability across different models and identified the main assumptions causing such differences (Dentener et al., 2006; Bain et al., 2017; Tan et al., 2018). The accuracy of any model in capturing wet deposition depends on the precursor emission inventory's accuracy, the distribution of cloud liquid water content (defining cloud Surface Area Density, SAD), the formation and distribution of aerosol particles, phase transfer, and parameterizations for dry/wet deposition.

94   The IFS-COMPO model is a large-scale global model used for operational analyses and air quality forecasts (Peuch
95   et al., 2022; Williams et al., 2022; Rémy et al., 2024) as part of the Copernicus Atmosphere Monitoring Service
96   (CAMS). This service provides forecasts and reanalyses of trace gases and aerosols to inform national service
97   providers and policymakers. It delivers chemical/aerosol forecast products, including ozone (O_3), nitrogen dioxide
98   (NO_2), SO_2, $PM_{2.5}$, PM_{10}, and aerosol optical depth. One of the recent updates to IFS-COMPO focused on reducing
99   biases and improving correlations for aerosol products (Rémy et al., 2024). As a result, acidic deposition and
100 nitrogen loading outputs from the model will likely improve as PM distribution accuracy increases, fostering the
101 development of future IFS-COMPO products.

102 This paper analyzes the regional performance of IFS-COMPO CY48r1 and CY49r1 in terms of surface
103 distributions of nitrogen and sulfur gaseous precursors for SIA, along with the associated particle concentrations
104 and distributions, evaluated against ground-based observation networks. Special emphasis is placed on the
105 application of the latest EQSAM4Clim updates (Metzger et al., 2024) in the global chemical forecasting model
106 IFS-COMPO CY49r1. This work complements a recent evaluation of the performance of IFS-COMPO CY48r1
107 and CY49r1 and the impact of using EQSAM4Clim with respect to regional $PM_{2.5}$ distributions and aerosol optical
108 depth, presented in Rémy et al. (2024). The influence of these updates on regional wet and dry deposition terms is
109 also evaluated to assess improvements to both EQSAM4Clim and the deposition schemes. Section 2 provides
110 details of the IFS-COMPO simulations used, a brief description of the latest model updates, and the emissions
111 used. Section 3 describes the observational networks against which surface evaluations are performed for precursor
112 gases and resulting SIA particulates. Section 4 details the changes in regional surface concentrations of precursor
113 gases and associated particulates, along with regional annual mean statistics. Section 5 presents the comparisons
114 of annual mean wet deposition fluxes for Europe, the U.S., and Southeast Asia, and discusses improvements.
115 Finally, Section 6 offers further discussion and conclusions from our study. Additional supporting information is
116 available in the supplementary material.

117 **2. Model description of IFS-COMPO versions**

118
119 The IFS-COMPO global composition model (formerly known as C-IFS) is used for operational air quality analyses
120 and forecasts as part of CAMS. The modeling and data assimilation framework is regularly updated. Since July
121 2023, IFS-COMPO has been based on CY48R1, using recently updated chemical and aerosol components for
122 near-real-time simulations of atmospheric composition (https://www.ecmwf.int/en/elibrary/, last accessed
123 21.07.23; Rémy et al., 2022; Williams et al., 2022). These updates have been shown to reduce biases in key
124 products such as O_3 and NO_2 compared to previous cycles (Huijnen et al., 2016; Huijnen et al., 2019). In this study,
125 we perform simulations using CY48R1 and compare them against a version of IFS-COMPO based on CY48R1,
126 but with updates to the atmospheric composition components to be included in CY49R1, which will be operational
127 in November 2024 (Rémy et al., 2024). These updates aim to improve the aerosol component, wet deposition
128 scheme, and description of pH in clouds and aerosols by applying the EQSAM4Clim approach (Metzger et al.,
129 2016; Metzger et al., 2024; Rémy et al., 2024). For brevity, we provide only a brief description of the updates
130 made to the wet deposition parameterization and the implementation of EQSAM4Clim in IFS-COMPO, which
131 determines surface deposition fluxes. A more comprehensive description of the CY49R1 updates is provided in
132 Rémy et al. (2024), and details of the EQSAM4Clim thermodynamic module are found in Metzger et al. (2024).

133
134 **2.1 Updates in IFS-COMPO CY49R1**

135 The CY49R1 version of IFS-COMPO is built on the previous operational cycle (CY48R1) and includes eight
136 distinct aerosol types with multiple bins for size segregation: sea salt, desert dust, organic carbon, black carbon,
137 SO_4^{2-}, fine and coarse NO_3^-, NH_4^+, and secondary organic aerosol. For CY49R1, updates have been made to the
138 aerosol component, including modifications to the description and properties of desert dust and sea salt. These
139 changes impact the resident lifetimes and long-range transport of each aerosol species. Modifications to the aerosol
140 optics description have also been implemented, improving simulations of aerosol optical depth (AOD) and the
141 Ångström exponent compared to regional observations (Rémy et al., 2024). The gas-phase chemistry, photolysis,
142 and dry deposition are identical to those described in Williams et al. (2022).

143 In CY49R1, EQSAM4Clim is used to estimate the gas/particle partitioning of the HNO_3-NO_3^- and NH_3-NH_4^+
144 systems and to provide an estimate of aerosol pH. The pH of aqueous solutions, aquated aerosols, and precipitation
145 is updated at each time step using the EQSAM4Clim approach, which accounts for additional cations (Ca^{2+}, Mg^{2+},
146 Na^+, K^+), anions (SO_4^{2-}, HSO_4^-, NO_3^-, Cl^-), and their solute interactions, as comprehensively described in Metzger
147 et al. (2012, 2016, 2024). This replaces the original pH estimate, which was based on summing the contributions
148 from dissolved CO_2 and strong acids (HNO_3, HSO_3^-, H_2SO_4, NO_3^-, and methane sulfonic acid), buffered by

149 dissolved NH₃. The contributions to solution pH from dissolved formic and acetic acids (HCOOH and CH₃COOH,
150 respectively) are also now included in CY49R1, as they have been shown to influence cloud droplet pH (Shah et
151 al., 2020). This update impacts phase transfer, speciation, and the subsequent aqueous-phase oxidation of SO_2 in
152 cloud droplets, which affects SO_4^{2-} formation. The loss of gas-phase species such as H_2O_2 and the corresponding
153 formation of SIA particles are also affected. Note that both the original (CY48R1) and updated (CY49R1)
154 approaches account for the dominant gaseous contributions to solution pH, namely SO_2, HNO_3, and NH_3.
155 Consequently, the differences in cloud pH are generally smaller than the changes in aerosol pH.

156 Below-cloud scavenging of gaseous precursors is also affected by solution pH (e.g., Seinfeld and Pandis, 2006).
157 In CY48R1, fixed values for cloud pH were used over land (pH = 5.0) and ocean (pH = 5.6), providing only limited
158 variability in regions affected by both high and low emissions. In CY49R1, the pH calculation is now coupled with
159 resident trace gas and aerosol concentrations, improving consistency within IFS-COMPO and providing variable
160 scavenging rates dependent on tropospheric composition.

161 In CY48R1, the wet deposition routines for aerosols and chemistry were distinct, though both utilized a scheme
162 adapted from Luo et al. (2019) for operational use. To ensure a consistent approach between aerosol and trace gas
163 wet deposition, and to simplify code maintenance, these separate implementations have been merged into a unified
164 routine. This new routine now represents the wet deposition processes for both aerosols and chemical species and
165 is executed with either chemical or aerosol tracers as inputs. Similar to CY48R1 and previous versions, the routine
166 in CY49R1 is executed twice: once for large-scale precipitation and once for convective precipitation. For
167 convective precipitation, the assumed precipitation fraction has been standardized to 0.05 (whereas in CY48R1, a
168 value of 0.1 was used for chemistry scavenging and 0.05 for aerosol scavenging).

169 Additional upgrades have been made for aerosol wet deposition as follows: (i) The aerosol activation
170 parameterization of Verheggen et al. (2007) has been implemented, which estimates the fraction of aerosols
171 scavenged through in-cloud processes as a function of temperature. It applies to mixed clouds, specifically for
172 temperatures between the freezing point and 233 K. For temperatures above 0°C, the consistency of the parameters
173 determining the fraction of aerosols subject to in-cloud wet deposition with the Verheggen parameterization results
174 has been verified. (ii) For below-cloud scavenging of aerosol species, scavenging rates have been updated to better
175 reflect particle size dependency, as described by Croft et al. (2009). This update includes adjustments to the below-
176 cloud scavenging parameters, which describe the efficiency with which aerosols are removed by rain and snow,
177 depending on species and size distribution. A below-cloud scavenging model has also been implemented.

178 **2.2 Setup of model simulations**

179 The IFS-COMPO simulations used to evaluate the impact of the atmospheric composition upgrades proposed
180 for cycle 49R1 on tropospheric composition, precursor gases, particle distributions, and wet deposition terms
181 employ both IFS cycles CY48R1 and CY49R1. Here, CY49R1 refers to IFS-COMPO cycle 48R1, including the
182 proposed updates to the aerosol/chemistry modules for IFS cycle 49R1. The meteorological component remains
183 the same across simulations and corresponds to CY48R1. The simulations presented here cover the year 2018,
184 with a one-month spin-up period. The vertical resolution uses 137 individual model levels, and the horizontal
185 resolution is TL511, corresponding to approximately 0.4° x 0.4°. These experiments do not include data
186 assimilation of observations. Meteorology is initialized every 24 hours based on ERA5 reanalysis data, meaning
187 IFS-COMPO is run in a cyclic forecast mode. A 15-minute chemical time step is used to solve a modified version
188 of the CB05 tropospheric chemistry scheme (Williams et al., 2022), excluding active stratospheric chemistry for
189 efficiency. Three-hourly, three-dimensional global output is used for the analysis.

190 The details of the sensitivity experiments are summarized in Table 1. The CY48R1 reference simulation pertains
191 to the 48R1 version of IFS-COMPO, while the CY49R1 simulation is based on the version described in Rémy
192 et al. (2024). The CY49R1_NOE4C simulation is identical to the CY49R1 simulation, except that the
193 EQSAM4Clim module (Metzger et al., 2016) is deactivated. For future reference, the experiment identities on
194 the ECMWF Multiversion Asynchronous Replicated Storage system (MARS) are hylm (CY48R1), i3bw
195 (CY49R1_NOE4C), and i3ad (CY49R1). These three simulations use a configuration similar to those described
196 in Rémy et al. (2024) for evaluating particulate matter (PM).

197 **Table 1:** Definitions of the IFS-COMPO simulations used in this study.

Simulation	Experiment ID	Comments

Geoscientific
Model Development
Discussions

CY48R1	hylm	Reference CY48R1 model version.
CY49R1	i3ad	As CY48R1, but with all composition modeling updates for CY49R1, particularly activating EQSAM4Clim in both aerosols and cloud droplets.
CY49R1_NOE4C	i3bw	As CY49R1, but with the EQSAM4Clim module deactivated.

198

199 The emissions used in these configurations are taken from the CAMS_GLOB_ANT v5.3 dataset (Soulie et al.,
200 2023), with biogenic emissions from the CAMS_GLOB_BIO v3.1 dataset (Sindelarova et al., 2022;
201 http://eccad.aeris-data.fr) and biomass burning emissions from GFAS v1.2 (Kaiser et al., 2012). All emissions
202 are applied using the methodology described in Ye et al. (2021). Apart from biomass burning (BB) and SO_2,
203 emissions are applied in the lowest model level. Currently, the emission of dimethyl sulfide (DMS) is based on
204 a climatology, i.e., it is not coupled to sea surface temperature, which controls biogenic activity (Deschaseaux
205 et al., 2019). Additionally, direct production of SO_4^{2-} and HNO_3 from hot shipping exhausts is not accounted
206 for.

207 **3. Observations**

208 For the evaluation of the regional distribution and concentrations of SIA precursor gases, as well as the associated
209 particle concentrations and deposition fluxes, we use data freely available from various observational networks.
210 Here, we provide only a brief description of the chosen networks.

211 For gas-phase precursors, we use in-situ measurements of SO_2 from the AirBase (Europe,
212 https://www.eea.europa.eu/, last accessed 12 Aug 2024), AirNow (U.S., https://www.airnow.gov/about-airnow/,
213 last accessed 12 Aug 2024), and the China National Environmental Monitoring Center (CNEMC,
214 https://www.cnemc.cn/) networks. Only rural background stations have been selected, and filtering has been
215 applied to the AirNow data to remove spurious high values that are not representative of rural background
216 conditions.

217 For $NH_3(g)$ in the U.S., we compare both weekly and yearly mean values derived from in-situ measurements taken
218 from selected stations participating in the Ammonia Monitoring Network (AMoN,
219 https://nadp.slh.wisc.edu/networks/ammonia-monitoring-network/, last accessed 12 Aug 2024), selecting 18
220 individual sites across the continent. No filtering has been applied to these measurements, as quality control has
221 been adopted from the provider.

222 For $HNO_3(g)$ in Europe and the U.S., we use data provided by the European Monitoring and Evaluation Programme
223 (EMEP, Torseth et al., 2012; https://ebas.nilu.no/, last accessed 12 Aug 2024) and the Clean Air Status and Trends
224 Network (CASTNET; https://www.epa.gov/castnet, last accessed 12 Aug 2024), respectively. For Southeast Asia,
225 data from the Acid Deposition Monitoring Network in East Asia (EANET, https://www.eanet.asia/, last accessed
226 14 Aug 2024) is used. However, no corresponding measurements of $NH_3(g)$ and $HNO_3(g)$ are available for the
227 Southeast Asia domain. For evaluating particle concentrations, we use available data from the CASTNET, EMEP,
228 and EANET networks for SO_4^{2-} and NO_3^-.

229 For wet deposition totals, we use data from the same measurement networks as those for the gaseous precursors,
230 thus removing any potential differences introduced by spatial sampling that might complicate the comparisons
231 discussed here. Specifically, these are the EMEP network for Europe, the CASTNET network for the U.S., and
232 the Acid Deposition Monitoring Network in East Asia (EANET, https://www.eanet.asia/, last accessed 14 Aug
233 2024) for Southeast Asia. No filtering of the data was performed before making the comparisons. Although
234 seasonal variability is of interest, the EANET wet deposition totals are only provided as annual mean values, which
235 limits the sampling frequency used for the analysis.

236 The averaging period chosen for the evaluation is primarily constrained by the availability of data from Southeast
237 Asia, which only provides annual mean values. For Europe and the U.S., data is provided on different timescales,
238 ranging from daily to weekly (CASTNET) and biweekly (AMoN). Averaging of model data is done using the
239 respective time intervals for each dataset to provide weekly composites at the selected stations used for SO_2, NH_3,
240 and HNO_3 comparisons.

Geoscientific
Model Development
Discussions

Open Access

EGU

4. The influence of pH on SIA chemical precursors and particulates

The efficacy of SIA formation is strongly governed by the concentrations of gaseous precursors. Therefore, changes introduced to the parameterizations for simulating particle formation also have feedback effects on the precursors, due to changes in fractional uptake governed by the solute pH. In this section, we evaluate the temporal and regional distribution, as well as biases, of both gaseous precursors (SO_2, NH_3, HNO_3) and SIA (namely SO_4^{2-}, NH_4^+, NO_3^-) simulated by IFS-COMPO for Europe, the U.S., and Asia. Mixing ratios and particle concentrations are strongly influenced by the description and distribution of primary emission sources, meteorology, deposition, aerosol pH (for NH_x and NO_x), and atmospheric transport. To investigate IFS-COMPO's ability to capture observed distributions, we present both weekly and annual mean comparisons for CY48R1 and CY49R1 against corresponding measurement composites. Given that the differences between CY48R1 and CY49R1_NOE4C are smaller (as shown in the budget analysis of gaseous precursors), we limit the selection of results for brevity. A direct link exists between [NH_4^+] and [NO_3^-] because the Nitrate#1 tracer takes the form of NH_4NO_3. All observational data are used to calculate the statistics, so they represent the mean across different chemical regimes. However, the location of sampling sites is not homogeneous throughout the analysis region, meaning results can be weighted towards certain states/countries. For Mean Bias (MB) and Root Mean Square Error (RMSE), negative percentage differences indicate improvements in bias statistics, whereas for Pearson's R, a positive percentage difference indicates improvement.

To assess the scale of these feedbacks, we show monthly mean regional differences for July and December 2018 for the three selected regions, focusing on SO_2, NH_3, and HNO_3. To evaluate the performance of IFS-COMPO, we aggregate data at a weekly frequency. For SIA, we present annual mean values against observations.

4.1 SO_2 and $SO_4^=$

Figure 1 shows weekly comparisons of surface $SO_2(g)$ concentrations ($\mu g/m^3$) from the three regions for 2018 against observational composites assembled from background/rural stations, as selected from the relevant observational networks introduced in Section 3. The associated annual mean statistics are provided in Table 2. In Europe, observations show typical weekly values of 0.5-1 $\mu g/m^3$ with no significant seasonal cycle, indicating the effective mitigation of SO_2 emissions in the region over the last few decades (Aas et al., 2024). In contrast, IFS-COMPO exhibits a seasonal cycle with an amplitude of 2 $\mu g/m^3$, driven by the monthly variability in the bottom-up emission inventories used. Typically, there is a positive bias in the simulations throughout the year, varying between 0.5 and 1 $\mu g/m^3$. A notable reduction in the wintertime bias of 0.5-1 $\mu g/m^3$ between CY48R1 and CY49R1_NOE4C (see Fig. 1A in the Appendix) indicates an increase in SO_4^{2-} production (quantified as a small increase, as shown in Table 3). For CY49R1, the MB with respect to surface [SO_4^{2-}] decreases by approximately 0.1-0.2 $\mu g/m^3$. The primary source of SO_2 being direct emissions suggests that emission estimates for Eastern Europe may be too high (see Fig. 1A in the Appendix). The annual MB value decreases by around 25%, with moderate correlation. In the U.S., weekly mean SO_2 values in the observations are typically around 2.5 $\mu g/m^3$, more than double those observed in Europe.

Figure A1 in the Appendix details the regional monthly mean distributions of surface SO_2 mixing ratios for July and December 2018 for CY48R1, along with percentage differences between CY48R1, CY49R1_NOE4C, and CY49R1. To assess the global integrated impact on SO_4^{2-} formation, the associated global budget terms are provided in Table 3 in Tg S/year. Comparing spatial distributions across regions, Europe exhibits the lowest SO_2 mixing ratios in CY48R1, reflecting strong mitigation practices over the last few decades (e.g., Vestreng et al., 2007). The maps for December show higher mixing ratios toward the east, with a significant contribution from shipping. In the U.S., a stark east-west gradient exists, governed by the continental distribution of anthropogenic emissions, with higher emissions toward the East Coast, again showing a seasonal signature. Maximal surface mixing ratios are 5-10 times higher than those simulated for Europe and are distributed over a much larger area. As expected, China exhibits the highest mixing ratios, between 10-20 ppb across the country, which is approximately 20 times higher than those simulated for Europe in both months shown.

Comparing CY48R1 against CY49R1_NOE4C reveals reductions in surface [$SO_2(g)$] across all regions of between 0-10%, leading to limited increases in SO_4^{2-} production of a few percent due to changes unrelated to aerosol and solution pH updates. This small increase in SO_4^{2-} production is reversed when applying the EQSAM4Clim pH methodology (Metzger et al., 2024), where the conversion efficacy of SO_2 is faster at more alkaline pH. The global budget terms show that, in addition to primary emissions, approximately one-third of SO_2

293 in the troposphere comes from the oxidation of dimethyl sulfide (DMS) by hydroxyl radicals (OH), with DMS
294 originating from biogenic activity in the oceans. In CY48R1, approximately 20% of SO_2 is oxidized in the gas
295 phase and 43% in the aqueous phase, with the remaining 37% lost to the surface via dry and wet deposition. This
296 increase in gas-phase production via OH is linked to changes in O_3-NO_x reaction cycles near anthropogenic source
297 regions, resulting in a small increase in O_3 of a few percent (not shown). The corresponding values for
298 CY49R1_NOE4C show changes of a few percent across terms, increasing the global burden by 1.5%, mostly in
299 the lower troposphere. For CY49R1, the application of EQSAM4Clim pH in cloud droplets reduces both the
300 uptake and oxidation of SO_2 by reducing aquated sulfite ($[SO_3^{2-}]$aq, $pKa(HSO_3^-) = 7.2$) and enhances gas-phase
301 oxidation due to increased OH, resulting in more gas-phase production of H_2SO_4, which is subsequently scavenged
302 into solution, further increasing solution acidity (lower pH values) in cases of excess SO_4^{2-} (i.e., insufficient
303 cations to completely neutralize all SO_4^{2-}).

304 **Table 2**: The annual Mean Bias (MB), Root Mean Square Error (RMSE), and Pearson's R values for weekly mean
305 regional distributions and concentrations of gaseous SO_2 compared against observational composites for 2018, as
306 shown in Figure 1, for Europe, the U.S., and China. For China, statistics relate to seasonal means.

| Diagnostic	Europe (EMEP)		US (CASTNET)		China (CNEC)	
	CY48R1	CY49R1	CY48R1	CY49R1	CY48R1	CY49R1
MB ($\mu g/m^3$) RMSE Pearsons R	0.85 0.48	0.77 0.49	-0.16 0.185	-0.26 0.192	11.6 0.07	11.5 0.07

307

308 **Table 3:** The tropospheric SO_2 budget in Tg S/year for 2018, as calculated by CY48R1, CY49R1_NOE4C, and
309 CY49R1, with the associated relative differences provided in parentheses (e.g., ((CY49R1 - CY48R1) / CY48R1)
310 * 100).

| Process	CY48R1	CY49R1_NOE4C	CY49R1
Emission	54.0	54.0 (-)	54.0 (-)
DMS + OH → SO_2	21.8	21.8 (-)	21.5 (-1.6)
SO_2 + OH → H_2SO_4	15.1	15.4 (+2.3)	16.5 (+9.3)
SO_2 (aq) → SO_4 (aq)	33.7	33.9 (+1.2)	33.0 (-2.2)
Dry Deposition	21.6	21.3 (-3.0)	22.2 (+3)
Wet Deposition	8.2	8.0 (-3.0)	6.9 (-15.8)
Burden	0.70	0.71 (+1.4)	0.75 (+7.1)
Lifetime (days)	3.25	3.29 (+1.2)	3.48 (+7.1)

311

312 Figure 1A shows that the region with the highest surface SO_2 concentrations is the northeastern U.S., with other
313 regions moderating the biases. There is little seasonality in the weekly observational composites. A positive bias
314 is observed during the winter and a negative bias during the summer, around 0.5-1.0 $\mu g/m^3$ across all simulations.
315 In CY49R1, the annual mean negative bias increases by approximately 0.1 $\mu g/m^3$, and there is poor correlation
316 with the observations. In China, weekly SO_2 concentrations are an order of magnitude higher than those observed
317 in the other regions, reaching 15-20 $\mu g/m^3$ during winter. The simulated concentrations exhibit a very large
318 positive bias, between 10-20 $\mu g/m^3$, suggesting that the regional SO_2 emissions in the global inventory are
319 significantly overestimated. Only negligible improvements are observed in CY49R1, where no detectable
320 correlation exists between the simulated and observed values.

321
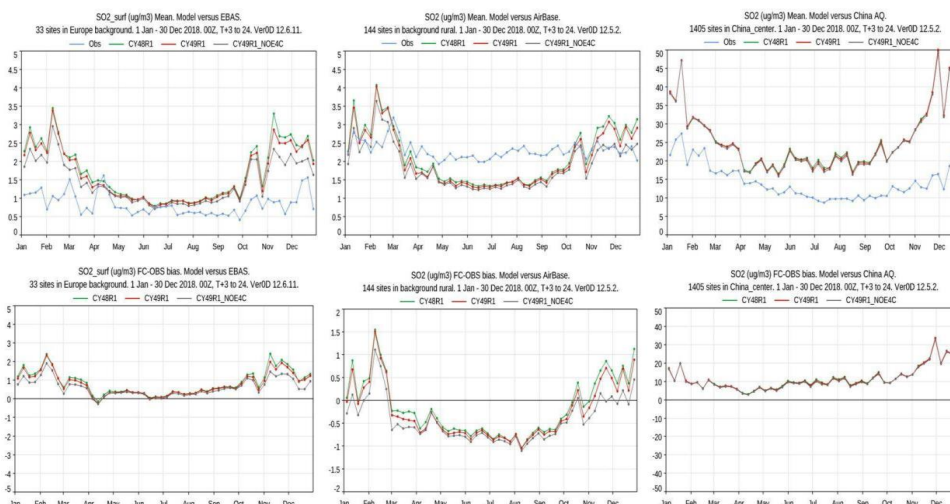
Figure 1: A comparison of weekly mean SO_2 concentrations for (a) Europe (AirBase, left), the U.S. (AirNow, middle), and China (CNEC, right), simulated in CY48R1 (green), CY49R1_NOE4C (grey), and CY49R1 (red), compared against measurement composites from stations representative of rural conditions in 2018.

Figure 2 compares weekly SO_4^{2-} surface concentrations in Europe, using data from the EBAS archive and IFS-COMPO simulations, along with associated biases. There is a seasonal cycle in the observational composites, with higher surface $[SO_4^{2-}]$ during winter, despite the weaker seasonal cycle for SO_2 (cf. Figure 1). The simulations show a weak seasonal cycle for surface SO_4^{2-}, with fairly constant values during the summer and low weekly biases. However, significant weekly biases occur in winter, where observations exhibit high variability. CY48R1 shows a low annual MB of -0.41 µg/m³, which is reduced in CY49R1_NOE4C (-0.20 µg/m³) and further in CY49R1 (+0.01 µg/m³). The correlation coefficient improves marginally, from 0.37 (CY48R1/CY49R1_NOE4C) to 0.43 (CY49R1).

332
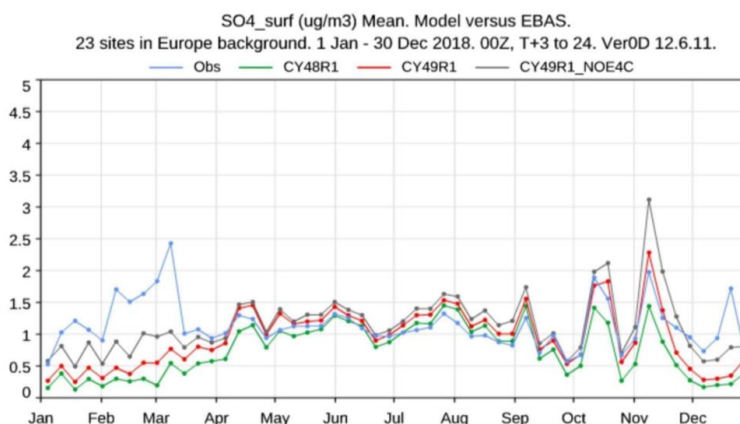
Figure 2: A comparison of weekly mean SO_4^{2-} for Europe (µg/m³) simulated in CY48R1, CY49R1_NOE4C, and CY49R1, compared against measurement composites from stations representative of rural conditions in 2018.

Figure A2 in the appendix shows the corresponding comparison against weekly observational composites of surface SO_4^{2-} from the CASTNET measurement network. No seasonal cycle is observed in the surface $[SO_4^{2-}]$ observations, with typical values around 0.7-1.0 µg/m³. During winter, lower weekly MB values are observed for both

339 CY49R1_NOE4C and CY49R1, with some degradation in weekly MB for certain weeks when applying
340 EQSAM4Clim. In summer, much larger positive biases occur, reaching 100-150% for all simulations due to the strong
341 seasonal cycle, with only marginal improvement in CY49R1 regarding weekly MB. The low MB for SO_2 shown in
342 Figure 1 suggests that the rate of oxidation in IFS-COMPO is too fast.

343 Figure 3 presents the annual mean surface $[SO_4^{2-}]$ for CY48R1 and CY49R1 for Europe, the U.S., and Southeast Asia.
344 The changes in surface $[SO_4^{2-}]$ are somewhat unaffected by the aerosol pH changes due to EQSAM4Clim, as shown
345 in Rémy et al. (2024) for 2019. This is because SO_4^{2-} production is dominated by aqueous-phase processes, with small
346 increases from organic acids. One key difference for SO_x is that SO_4^{2-} production is irreversible, depending on cloud
347 pH, dissolved O_3, and hydrogen peroxide (H_2O_2).

348 In Europe, sampling sites for this aerosol species in the EMEP network are such that comparisons for southern
349 European countries are excluded from the regional mean statistics. A sharp north-south gradient exists, driven by
350 variability in H_2SO_4 production between seasons, cloud cover for the wet production term, and the distribution of
351 primary SO_2 emission sources. Mitigation measures have reduced the increase in emitted fluxes during winter months
352 associated with domestic heating (Versteeg et al., 2007). Simulated concentrations in CY48R1 are lower in Scandinavia
353 compared to countries like France, resulting in a low bias of around 1 µg/m³ in Finland and around the Baltic, related
354 to missing shipping emissions. In other European sites, the agreement is better, with the low bias decreasing to
355 approximately 0.5 µg/m³. One outlier exists at the most easterly station, which exhibits a significant high bias of 1.5
356 µg/m³. In CY49R1, simulated surface $[SO_4^{2-}]$ increases by 0.2-0.4 µg/m³, leading to improved bias, as shown in Table
357 7. However, only small improvements are made to the correlation coefficient due to identical emission estimates and
358 the fact that SO_x is the least affected by EQSAM4Clim, impacted only indirectly through changes in pH.

359 In the U.S., CASTNET observations show an east-west continental gradient in surface $[SO_4^{2-}]$, determined by the
360 distribution of primary SO_2 emissions and transport (cf. Figure A1). There is a significant transport component for
361 SO_4^{2-}, with surface $[SO_4^{2-}]$ in the marine boundary layer ranging from 1.0-2.5 µg/m³, where transport dominates local
362 surface $[SO_4^{2-}]$ produced from DMS oxidation (Simpson et al., 2014). In CY49R1, surface $[SO_4^{2-}]$ decreases at the
363 continental scale, reducing the annual MB from 0.67 to 0.20 µg/m³, with a corresponding increase in the correlation
364 coefficient to 0.43, although it remains weakly correlated.

365 In the western U.S., a positive MB is introduced for rural background sites in CY49R1, ranging from 0.5-0.7 µg/m³,
366 with a contribution from transport from the east. Therefore, reductions in the annual MB are driven by lower biases
367 related to eastern sampling stations. The positive MB of approximately 1-1.5 µg/m³ around Kentucky/Tennessee
368 suggests that local SO_2 emission estimates may be too high (see Discussion in Section 5).
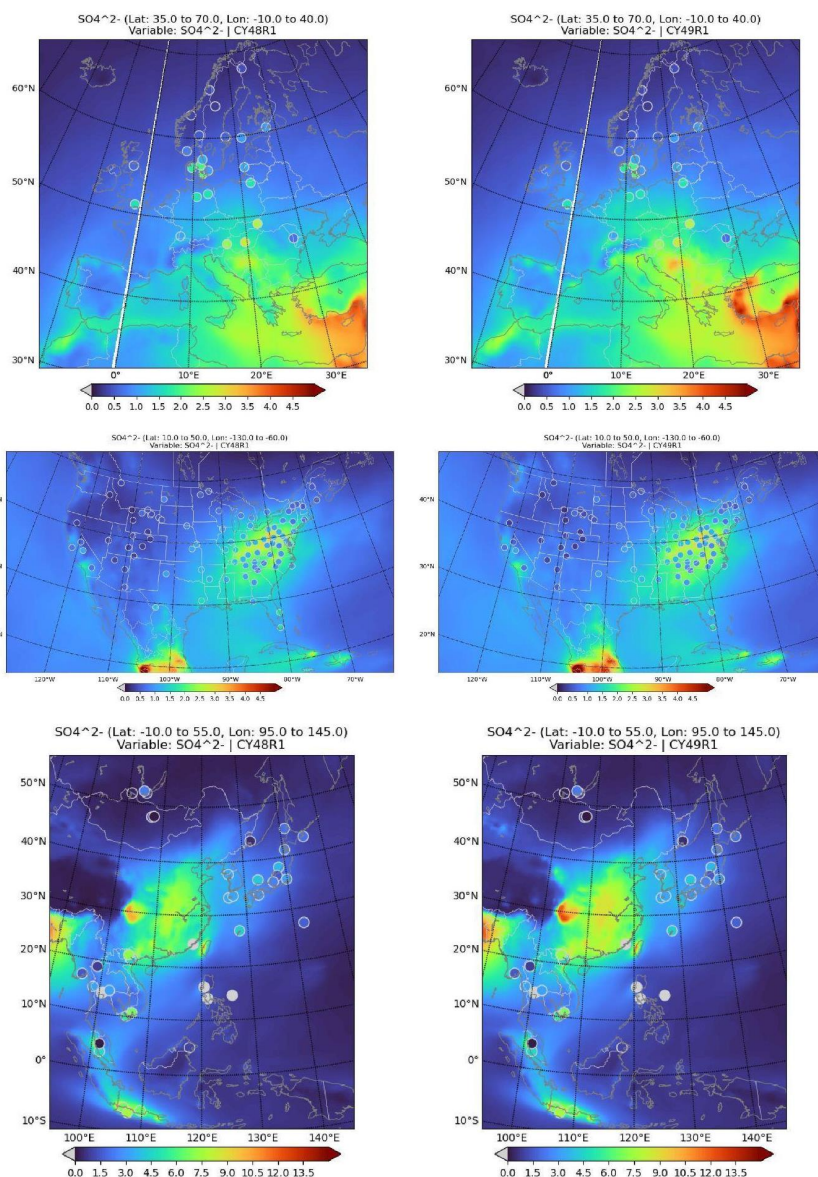
Figure 3: Comparisons of annual mean [SO$_4^{2-}$] simulated in CY48R1 and CY49R1 compared to measurements for the three selected regions, given in µg/m³.

In Asia, the scarcity of sampling sites in the EANET network results in a less robust evaluation. Many sampling sites are located on the coast rather than inland, so changes in coastal regions significantly influence regional statistics. Higher primary SO$_2$ emissions occur inland. Therefore, any positive MB near source regions is not included in the statistics; the results shown here for surface SO$_4^{2-}$ should be considered lower limits. Long-range transport of SO$_4^{2-}$ in Asia has been shown to partially neutralize national SO$_2$ mitigation measures, such as those in Taiwan and South Korea. This originates from changing trends in SO$_2$ emissions from mainland China, as captured by EANET measurement sites (Chang et al., 2022). For CY48R1, the annual mean statistics show a very low MB and a good correlation coefficient of 0.75. However, in CY49R1, performance degrades, with the MB increasing to 0.48 µg/m³, showing a trend similar to that in the U.S. Notably, more remote sampling stations (e.g., oceanic) exhibit regional

10

381 negative biases (approximately -0.7 µg/m³), while sites near Mongolia and South Korea agree well, with low MB
382 values. In Thailand and Vietnam, large MB values suggest that regional SO_2 emission estimates are too high.
383 Unfortunately, there are no in-situ measurements available for better quantification. The correlation coefficient
384 degrades in CY49R1 compared to CY48R1, dropping to 0.66. Overall, improvements in the SO_2-SO_4^{2-} couple are
385 mixed and less pronounced compared to other SIA species.

386 **Table 4**: The annual MB, RMSE, and Pearson's R values for daily (EMEP, Europe), weekly (CASTNET, U.S.), and
387 annual (EANET, Southeast Asia) mean regional distributions and concentrations of surface SO_4^{2-} compared to
388 observational composites for 2018 shown in Figures 8-10 for Europe, the U.S., and Southeast Asia. Percentage
389 differences are calculated as ((CY49R1 - CY48R1) / CY48R1) * 100.

	Europe (EMEP)		US (CASTNET)		SE Asia (EANET)	
$SO_4^=$	CY48R1	CY49R1	CY48R1	CY49R1	CY48R1	CY49R1
MB (ug/m³)	-0.49	-0.32 (-35)	0.67	0.20 (-70)	-0.02	0.48 (+96)
RMSE	1.35	1.31 (-3)	0.93	0.46 (-50)	1.64	2.28 (+39)
Pearsons R	0.45	0.47 (+4)	0.33	0.43 (+23)	0.75	0.66 (-12)

390

391 **4.2 NH_3 and NH_4^+**

392 Figure 4 compares weekly observational composites of $[NH_3(g)]$ from the EBAS archive against data extracted from
393 the various IFS-COMPO simulations for 2018. The observational composite shows a skewed seasonal cycle, with a
394 maximum in April due to agricultural activity. Wintertime values are around 0.5 µg/m³, increasing to 1.0-2.0 µg/m³
395 during spring and summer. This seasonal variability is captured across all simulations, albeit with a significant positive
396 summertime weekly bias of 1-2 µg/m³ in CY48R1 (annual MB: 1.04 µg/m³). A small increase in bias is simulated for
397 CY49R1 (annual MB: 1.21 µg/m³). There is high correlation across simulations, with values ranging from 0.71-0.73.
398 The occurrence of weekly increases in observed values is typically captured by IFS-COMPO, but there is a modest
399 degradation in performance compared to CY48R1.

400 The regional distribution of surface NH_3 for 2018 in the three chosen regions, and the changes resulting from both the
401 IFS cycle upgrades and the application of EQSAM4Clim, are shown in Figure A2 in the Appendix. The corresponding
402 global chemical budget terms are provided in Table 5. Despite a declining trend in European regional NH_3 emissions
403 (Tich? et al., 2023), a strong seasonal cycle exists in CY48R1. Maximal mixing ratios are found around Benelux and
404 northern Italy, with local differences of 8-20 ppb between July and December across regions. The
405 CAMS_GLOB_ANT v5.3 (Soulie et al., 2023) emission inventory has recently been validated for NH_3 against top-
406 down estimates, providing confidence in the estimates' quality (Ding et al., 2024). In the U.S., a similar seasonal
407 signature exists, especially in the northwest and southeast, associated with agricultural emissions (Wang et al., 2020),
408 with background mixing ratios of 0.5-2.0 ppb remaining relatively constant.

409 In China, where NH_3 emissions have increased over recent decades (Liu et al., 2019; Chen et al., 2023), surface mixing
410 ratios of 5-20 ppb occur in July over large areas, again associated with agricultural practices. Similarly, high mixing
411 ratios are observed around Bangladesh (> 20 ppb). In December, mixing ratios are typically an order of magnitude
412 lower, except in the southwest, where high mixing ratios (> 20 ppb) persist. Measurements of NH_x over the ocean are
413 rare, so the large increases shown cannot be verified. Nevertheless, estimates range from 0.1-4.2 ppb depending on
414 season and location (Sharma et al., 2012), indicating a significant negative bias in CY48R1 that is somewhat improved
415 in CY49R1.

416 **Table 5**: The tropospheric NH_3 budget in Tg N/year for 2018, as calculated by CY48R1 and CY49R1, with relative
417 differences shown as (CY49R1-CY48R1)/CY48R1.

Process	CY48R1	CY49R1_NOE4C	CY49R1
Emission	51.1	51.1 (-)	51.1 (-)
NH_3 + OH	0.82	0.99 (+20)	1.98 (+240)

$NH_3 \rightarrow NH_4^+$	30.6	30.3 (-1)	17.3 (-44)
Dry Deposition	16.3	16.6 (+2)	22.4 (+37)
Wet Deposition	7.0	6.2 (-13)	10.6 (+51)
Burden	0.13	0.16 (+19)	0.29 (+118)
Lifetime (days)	0.9	1.1 (+22.0)	2.0 (+133)

418

419
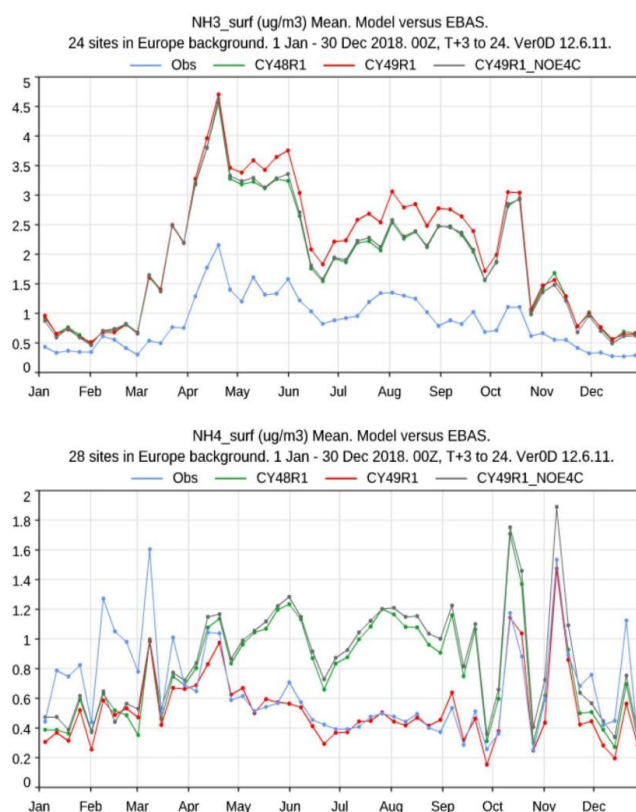
Figure 4: A comparison of weekly mean [NH_3(g)] and [NH_4^+] at the surface for Europe (µg/m³), simulated in CY48R1 (green), CY49R1_NOE4C (grey), and CY49R1 (red), compared against measurement composites from stations representative of a rural scenario for 2018. The corresponding biases are shown in the bottom panel.

Comparing CY48R1 and CY49R1_NOE4C shows decreases of 5-20% over land in the chosen regions. Changes in [NH_4^+] production are minimal in the absence of EQSAM4Clim, with most NH_3(g) lost through conversion to NH_4^+. In CY49R1_NOE4C, there is a 13% decrease in the dissolved fraction of NH_3, which is subsequently lost as wet deposition, contributing to a nearly 20% increase in the tropospheric NH_3 burden. This is attributed to changes in scavenging and wet deposition. In CY49R1, improved gas/particle partitioning from EQSAM4Clim reduces particle-phase concentrations of semi-volatile aerosol species, increasing gas-phase concentrations and affecting aerosol pH, which governs NH_3(g) solubility. This reduces its conversion into NH_4^+ (see Table 5, approx. 44% reduction), amplified by the inclusion of mineral cations (Ca^{2+}, Na^+, K^+, Mg^{2+}). The tropospheric lifetime of NH_3 more than doubles in CY49R1, in line with changes in the tropospheric burden. Both dry and wet deposition increase (by 37% and 51%, respectively) due to lower NH_4^+ particle production.

433 Figure 4 also presents weekly comparisons of observational composites of [NH$_4^+$] at the surface from the EBAS
434 archive against IFS-COMPO simulations for 2018. Although maximum observed NH$_3$(g) in Figure 4 occurs in May,
435 higher [NH$_4^+$] is observed during winter. Both CY48R1 and CY49R1_NOE4C exhibit summertime mean biases of >
436 100% (0.5 µg/m³), which are removed in CY49R1 by applying EQSAM4Clim, resulting in a very low bias (< 0.1
437 µg/m³). This potentially improves PM2.5 and PM10 forecasts significantly by reducing cumulative bias across aerosol
438 types (see Rémy et al., 2024).

439 Similar comparisons are shown in Figure A5 in the Appendix for the U.S., using weekly composites from CASTNET
440 data. Unlike the seasonal cycle for [NH$_3$(g)], which peaks in May (see Fig. A4), weekly [NH$_4^+$] values peak in July,
441 remaining fairly consistent between 1.5-1.75 µg/m³ during summer. This suggests saturation in NH$_4^+$ particle
442 formation, likely linked to the availability of HNO$_3$(g) (cf. Fig. A7 in the Appendix). Significant biases exist in
443 CY48R1 and CY49R1_NOE4C, reaching 1.25 µg/m³ during summer (600% of observational values). Applying
444 EQSAM4Clim halves this positive bias in CY49R1, resulting in better agreement during winter.

445 A comparison of weekly [NH$_3$(g)] variability between IFS-COMPO and measurements from rural AMON sites in
446 2018 is shown in Figure A5 in the Appendix, with site details provided in the figure legend. Sites were selected to
447 cover a wide area of the U.S. Measurements show that winter [NH$_3$(g)] concentrations are lower than summer
448 concentrations across most sites, except in California, where seasonal temperature variability (and agricultural
449 practices) is less pronounced. Maximal concentrations range from 1-6 µg/m³, occurring during spring (Alabama/New
450 York) or summer (Florida), depending on the extent and timing of agricultural activity in each state. Differences
451 between CY48R1 and CY49R1_NOE4C are negligible, but weekly bias is significantly reduced in CY49R1. Arizona
452 is an exception, where a large positive bias suggests a too-high local emission flux. In CY49R1, high [NH$_3$(g)] also
453 depends on local [HNO$_3$(g)] via NO$_x$, the other important precursor for [NH$_4$(NO$_3$)] (cf. New York vs. Alabama). The
454 seasonality of weekly variability is well captured, with substantial improvements in cycle amplitude in CY49R1.

455 The corresponding statistics for 2018 against AMoN composites for all three simulations are shown in Table A2 in
456 the Appendix. Differences between CY48R1 and CY49R1_NOE4C in the U.S. are not appreciable (cf. Figure A2),
457 despite the global increase in the tropospheric NH$_3$ burden in Table 4. Without the aerosol pH changes in
458 EQSAM4Clim, limited repartitioning occurs. Therefore, further discussion is limited to changes in CY49R1 statistics.
459 The negative annual MB in CY49R1 is approximately half that in CY48R1, decreasing to 0.26 µg/m³, reflecting NH$_x$
460 repartitioning into NH$_3$(g) at higher aerosol pH, with a modest improvement in the correlation coefficient.

461 Figure 5 presents the annual mean [NH$_4^+$] distribution for Europe, the U.S., and Southeast Asia in CY48R1 and
462 CY49R1 during 2018, with regional annual mean statistics in Table 6. Measurement site locations are also shown,
463 with respective annual mean values within each circle. Significant decreases in NH$_3$ conversion in CY49R1 result in
464 lower [NH$_4^+$] concentrations, driven by improved gas/aerosol partitioning and increased aerosol pH when applying
465 EQSAM4Clim (see Table 4; Rémy et al., 2024). NH$_3$(g) depositional loss to the surface increases in CY49R1 due to
466 its longer residence time. Aerosol pH varies widely between regions, with Europe exhibiting values of 3-4, while the
467 southern U.S. and northern China exhibit pH values of 2-3 (Pan et al., 2024; Rémy et al., 2024), indirectly affecting
468 NH$_4^+$ production variability. Once formed, regional transport contributes to the continental distribution of NH$_4^+$ away
469 from strong source regions (Simpson et al., 2010; Renner and Wolke, 2010; Du et al., 2020).

470 In Europe, most observational annual mean values are between 0.2-1.2 µg/m³, exceeded by > 50% in CY48R1. In
471 CY49R1, annual mean [NH$_4^+$] decreases by 0.5-1.0 µg/m³, resulting in low annual mean [NH$_4^+$] values for Spain and
472 the UK, while reducing maximal concentrations by approximately 50% in northern Italy. This contributes to a
473 reduction in cumulative PM2.5 bias in the region, as shown in Rémy et al. (2024) for 2019. The associated MB values
474 in Table 6 show a significant bias reduction (> 80%) and an increase in the correlation coefficient, although the
475 simulated NH$_4^+$ distribution is still only moderately correlated (r=0.62). Unfortunately, no available measurements
476 allow for quantification of IFS-COMPO performance around the Mediterranean. It should be noted that with a more
477 realistic distribution and seasonal variability in NH$_3$(g) emissions (Shepard et al., 2011; Dammers et al., 2019), the
478 [NH$_4^+$] distributions would likely not be affected, as other SIA species govern NH$_3$-NH$_4^+$ gas/aerosol partitioning (see
479 Discussion).

480 In the U.S., similar decreases in annual mean [NH$_4^+$] values occur in CY49R1, with very low concentrations (0.1-0.4
481 µg/m³) in the western U.S., reducing bias compared to observational mean values. This reduces the annual mean
482 regional bias by approximately 0.7 µg/m³, as shown in Table 6. A gradient exists in aerosol pH from EQSAM4Clim,
483 with values ranging from pH 3.0 in the northwest U.S. to more acidic values of pH 2.0 in the southwest (Rémy et al.,
484 2024). This reduces NH$_3$(g) transfer, thus moderating NH$_4^+$ production (cf. Table 4). In the northeast U.S., with high

485 NO$_x$ emissions, reductions of 0.5-1.0 µg/m³ occur. In the southwest U.S., with high [NH$_3$(g)] from agriculture (cf.
486 Figure A2), reductions of 0.3-1.0 µg/m³ are observed. The correlation coefficient degrades, showing a moderate
487 annual mean correlation with significant overestimates in the southwest U.S., as shown in comparisons of [NH$_3$(g)]
488 at selected sites in Figure 6.

489 In Southeast Asia, simulated annual mean [NH$_4^+$] over land is typically much higher than in Europe or the U.S., with
490 maximal values of 7.0-9.0 µg/m³ in eastern China, despite similar surface NH$_3$(g) mixing ratios between Europe and
491 China (see Figure A3). This difference is driven primarily by higher HNO$_3$(g) in China, due to a more polluted
492 chemical regime (O$_3$, NO$_2$, and OH determine gas-phase HNO$_3$ production). Applying EQSAM4Clim in CY49R1
493 reduces [NH$_4^+$] by 1-2 µg/m³, particularly where annual mean [NH$_4^+$] exceeds 6.0 µg/m³. This reduces the annual
494 mean regional bias by 0.4 µg/m³, with a corresponding reduction in correlation due to less transport. The lack of
495 sampling sites in regions with high primary NH$_3$(g) emissions skews the annual mean biases. In more remote locations
496 (e.g., Mongolia/South China Sea), low values of < 0.5 µg/m³ are well captured in both CY48R1 and CY49R1.

497 **Table 6** As for Table 4, but for NH$_4^+$.

	Europe (EMEP)		US (CASTNET)		SE Asia (EANET)	
NH$_4^+$	CY48R1	CY49R1	CY48R1	CY49R1	CY48R1	CY49R1
MB (ug/m³)	0.26	-0.05 (-81)	0.95	0.23 (-48)	0.96	0.55 (-43)
RMSE	0.94	0.72 (-23)	1.71	0.46 (-73)	1.73	1.30 (-25)
Pearsons R	0.46	0.62 (+29)	0.59	0.43 (-27)	0.59	0.44 (-25)

498

499
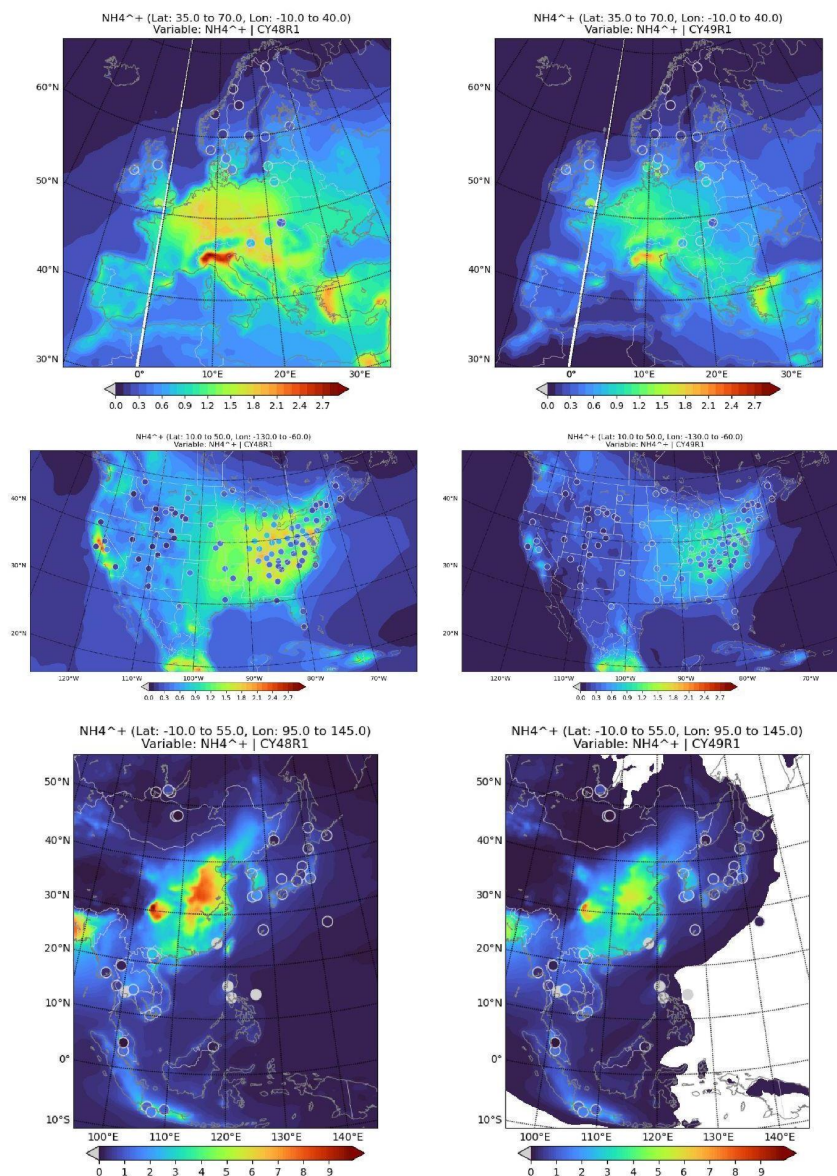
Figure 5: Comparisons of annual mean surface NH$_4^+$ particle concentrations simulated in CY48R1 and CY49R1, compared to measurements for the three selected regions during 2018 (µg/m³). The corresponding regional statistics are provided in Table 7.

15

4.3 HNO$_3$ and NO$_3^-$

508

509 Figure 6 shows the resulting changes in surface [HNO$_3$(g)] between simulations, compared against weekly
510 composites assembled from a selection of background measurement sites in Europe that participate in the EMEP
511 measurement network. The location of the sampling sites results in a significant bias towards northern Europe, where
512 seasonality is more pronounced. However, the observations exhibit only a weak seasonal cycle, with weekly values
513 ranging from 0.4-0.8 µg/m³, as many sites are located away from strong NO$_x$ sources. Both CY48R1 and
514 CY49R1_NOE4C (see Figure A7) show negative biases, underestimating concentrations by around 100% during
515 summer. In CY49R1_NOE4C, there is a bias reduction of approximately 0.1-0.2 µg/m³, indicating that other changes
516 made between IFS cycles cause alterations in the gas-phase production term in addition to the changes in NH$_4$NO$_3$
517 from EQSAM4Clim (cf. Table 8). In CY49R1, there is a significant excess of [HNO$_3$(g)] due to enhanced production
518 and reduced transfer into the particulate phase, despite an increase in cumulative deposition terms. Such changes are
519 associated with relatively low [HNO$_3$(g)] values in IFS-COMPO, around < 0.1 ppb (see Figure A7).

520 Figure A7 in the Appendix shows the monthly mean regional distribution of HNO$_3$(g) for July and December 2018
521 for the three selected regions for CY48R1, along with percentile differences when compared with CY49R1_NOE4C
522 and CY49R1. The corresponding global chemical budget terms for HNO$_3$(g) are provided in Table 7. No direct
523 emission of HNO$_3$ occurs in IFS-COMPO, as is often prescribed in global chemistry transport models to represent
524 chemistry in ship plumes. Instead, the main source is the oxidation of NO$_2$ by OH in the gas phase, as shown in
525 Table 7. This production term increases by approximately 14% in CY49R1 due to enhanced OH from changes in O$_3$
526 (not shown). For heterogeneous conversion, the cumulative HNO$_3$ production term is approximately 50% that of the
527 gas-phase production term, remaining relatively constant between simulations. A shift occurs between fine mode
528 NO$_3^-$ (NH$_4$NO$_3$) and coarse mode NO$_3^-$ (CaNO$_3$/NaNO$_3$), strengthening the link between NH$_4^+$ and NO$_3^-$ in IFS-
529 COMPO. Both dry and wet loss terms increase significantly due to the increased availability of HNO$_3$(g), reducing
530 the fraction converted to NO$_3^-$. The temporal variability of HNO$_3$(g) is influenced by the magnitude and extent of
531 regional NO$_x$ emissions, photochemical activity (via OH formation), gas/aerosol partitioning (where particles with
532 high SO$_4^{2-}$ content have an associated low NO$_3^-$ content), and scavenging in clouds and aerosols.

533 In Europe, very low surface mixing ratios occur over land during both months in CY48R1 (< 0.1 ppb), which is
534 surprising given that Benelux is known for high NO$_x$ levels (van der A, 2024), suggesting correspondingly high
535 HNO$_3$(g) mixing ratios. Higher mixing ratios of 0.25-0.5 ppb occur around the coasts and the Mediterranean,
536 originating from direct shipping emissions. This can lead to elevated NO$_3^-$ concentrations due to the uptake of
537 HNO$_3$(g) on sea salt, which may be overestimated, as EQSAM4Clim currently assumes thermodynamic equilibrium
538 without accounting for dynamic limitations. A coupling with a dynamic aerosol model is foreseen. In contrast,
539 applying EQSAM4Clim in CY49R1 results in large increases in surface HNO$_3$(g) at the continental scale during
540 July. In December, strong latitudinal variability occurs, with decreases of 25-75% in HNO$_3$(g) at latitudes higher
541 than 60°N, due to lower temperatures and lower RH in a relatively low NO$_x$ environment.

542 In the U.S., the highest HNO$_3$(g) mixing ratios in CY48R1 occur in the eastern states and California (1-2 ppb), with
543 much lower values in the more remote central U.S. (0.1-0.2 ppb), and a strong seasonal cycle with maximum values
544 peaking in July. Comparing the relative differences between simulations shows a significant increase in surface
545 HNO$_3$(g) in CY49R1 (100-6000 ppt) across the continent for both months, with the largest increases occurring in
546 the northern states. In contrast to Europe, no seasonal decreases are observed at any location.

547 In Southeast Asia, surface mixing ratios are the highest across all regions, with maximum values of 4-5 ppb along
548 the eastern coast (July) and in central regions (December). Comparing the relative differences between simulations
549 shows significant increases of 50-5000%, except in the more remote northern regions. As in Europe, strong
550 seasonality is observed, with decreases above 30°N, regardless of the NO$_x$ regime. As shown for NH$_3$ (see Figure
551 A3 in the Appendix), significant increases in HNO$_3$ over the ocean occur for both months, associated with lower
552 [NO$_3^-$] (as shown by the cumulative 50% reduction in global conversion).
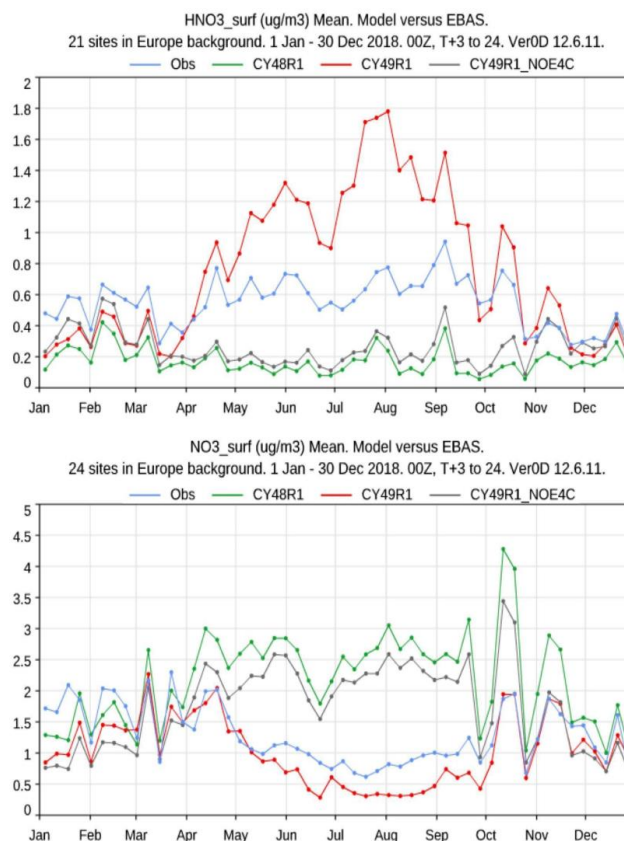
Figure 6: A comparison of weekly mean [HNO₃(g)] and [NO₃⁻] for Europe (µg/m³) at the surface, simulated in CY48R1 (green), CY49R1_NOE4C (grey), and CY49R1 (red), compared against measurement composites from stations representative of a background scenario in 2018. The evolution of the corresponding bias values is shown in the bottom panel.

Comparisons of weekly [HNO₃(g)] from the CASTNET measurement network in the U.S. are shown in the top panel of Figure A8 in the Appendix and reveal similar conclusions. As in Europe, both the concentrations and seasonal variability in the observations are low, with typical weekly concentrations around 0.5 µg/m³. The relatively even distribution of measurement sites in the U.S. means that the evaluation presented does not have significant regional bias. It is surprising that measured weekly mean concentrations are relatively constant, given that variability in the gas-phase chemical production term involves OH, which exhibits strong seasonality due to day length differences. In contrast to Europe, both CY48R1 and CY49R1_NOE4C show moderately good agreement with the measurements, with weekly biases around 0.2-0.25 µg/m³. However, CY49R1 introduces a large positive bias from EQSAM4Clim due to a limitation in HNO₃'s ability to condense on particle surfaces, as condensed HNO₃ does not contribute to NH₄NO₃ formation (this requires coupling EQSAM4Clim with a dynamic aerosol model, as described in Metzger et al., 2018). It also shows that although cumulative global dry and wet deposition terms in CY49R1 have increased markedly compared to CY48R1 (cf. Table 8), this is insufficient to compensate for the reduced aerosol formation.

The bottom panel of Figure 6 shows the corresponding changes in surface [NO₃⁻] for Europe, similar to the changes for HNO₃. Typical [NO₃⁻] values are almost twice those of [HNO₃(g)]. Unlike for HNO₃(g), a concave seasonal cycle is evident in the weekly observational composites, with lower concentrations of around 1 µg/m³ during summer compared to winter. Both CY48R1 and CY49R1_NOE4C fail to capture the correct seasonality, showing higher concentrations in summer, resulting in substantial positive biases of 1-2 µg/m³. The associated biases in [HNO₃(g)] indicate that the HNO₃-NO₃⁻ partitioning is poorly captured. In CY49R1, the seasonal cycle description

17

577 is improved by EQSAM4Clim, resulting in much lower biases (< 0.5 µg/m³) throughout the year, highlighting the
578 importance of better gas/particle partitioning representation. The bottom panel of Figure A8 in the Appendix shows
579 the corresponding changes in $[NO_3^-]$ against weekly composites from the CASTNET measurement network.
580 Strong similarities are seen with the improvements observed in the European comparison. In CY48R1 and
581 CY49R1_NOE4C, no seasonal variability occurs in $[NO_3^-]$, leading to significant positive biases of 1.5-2.0 µg/m³.
582 In CY49R1, biases decrease by an order of magnitude, and seasonal variability improves markedly.

583 **Table 7:** The tropospheric HNO₃(g) budget in Tg N/year for 2018, as calculated by CY48R1 and CY49R1, with
584 relative differences shown as (CY49R1 - CY48R1)/CY48R1.

Process	CY48R1	CY49R1_NOE4C	CY49R1
$NO_2 + OH \rightarrow HNO_3$	11.0	11.6 (+5)	12.6 (+14)
$N_2O_5 + Liq \rightarrow HNO_3$	2.2	2.5 (+12)	2.6 (+17)
$N_2O_5 + Aer \rightarrow HNO_3$	3.2	2.3 (-28)	2.3 (-27)
$NO_3 + Aer \rightarrow HNO_3$	0.8	0.4 (-47)	0.5 (-42)
$HNO_3 \rightarrow$ Fine NO_3-	1.4	1.2 (-18)	2.0 (+41)
$HNO_3 \rightarrow$ Coarse NO_3-	9.3	5.9 (-36)	3.6 (-17)
Dry Deposition	2.0	2.4 (+17)	5.1 (+150)
Wet Deposition	6.8	5.9 (-13)	9.3 (+38)
Trop. Burden	0.31	0.30 (-3)	0.32 (+3)

585

586 In Figure 7, we show the regional distributions of annual mean $[NO_3^-]$ for CY48R1 and CY49R1 during 2018 for
587 the three chosen regions, with the associated changes in regional annual mean statistics provided in Table 8. Some
588 commonality exists between the changes shown for annual mean $[NH_4^+]$ and $[NO_3^-]$, due to the speciation of the
589 SIA involved. The cumulative sums of smaller nitrate particles (fine mode NO_3^- in Table 4, in the form NH_4NO_3)
590 and larger nitrate particles (coarse mode NO_3^- in Table 4, in the form of $CaNO_3$ and $NaNO_3$) are included in the
591 plots. Therefore, the changes evaluated here represent a combination of changes in both fine and coarse mode
592 NO_3^-, rather than changes in individual particle sizes. Unlike the reduced nitrogen analysis provided above, which
593 is impacted more directly by changes in fine mode NO_3^-, $[NO_3^-]$ is also indirectly affected by coarse mode
594 assumptions through the effect of cations on neutralization levels, which subsequently control gas/aerosol
595 equilibrium partitioning. Changes in HNO₃ partitioning result in a reduction of NO_x in particulate form, due to a
596 higher dry deposition component.

597 In Europe, the simulated annual mean $[NO_3^-]$ in CY48R1 generally ranges from 0.2-1 µg/m³ over Scandinavia,
598 Spain, and surrounding seas, and from 2-6.3 µg/m³ over northwestern and central Europe and the Mediterranean,
599 with lower values towards the northeast and southwest. The highest European NO_x emissions occur in the southeast
600 UK, Benelux, the Ruhr, and Po valleys (e.g., Liu et al., 2021; van der A, 2024). This, and the relatively
601 homogeneous distribution within central Europe, shows significant transport once NO_3^- particles are formed. No
602 such continental gradient in annual mean $[NO_3^-]$ exists in the observational mean values, indicating an
603 overestimate in IFS-COMPO. Nevertheless, in CY49R1, decreases of 2-4 µg/m³ in $[NO_3^-]$ occur for the Baltic
604 states, France, Germany, and the Mediterranean Sea (from relatively high shipping NO_x emissions), resulting in
605 better agreement with the annual mean observed values at individual measurement stations. The annual regional
606 MB decreases by ~90%, dropping to 0.1 µg/m³ in CY49R1, with an associated increase in the correlation
607 coefficient due to lower transport of $[NO_3^-]$ out of the main source regions. A large impact is observed due to the
608 acidification of sea salt aerosols under relatively high NO_x emissions from dense shipping lanes, which can be seen
609 by the similar $[NO_3^-]$ reductions over the sea, though these are difficult to evaluate due to insufficient
610 measurements.
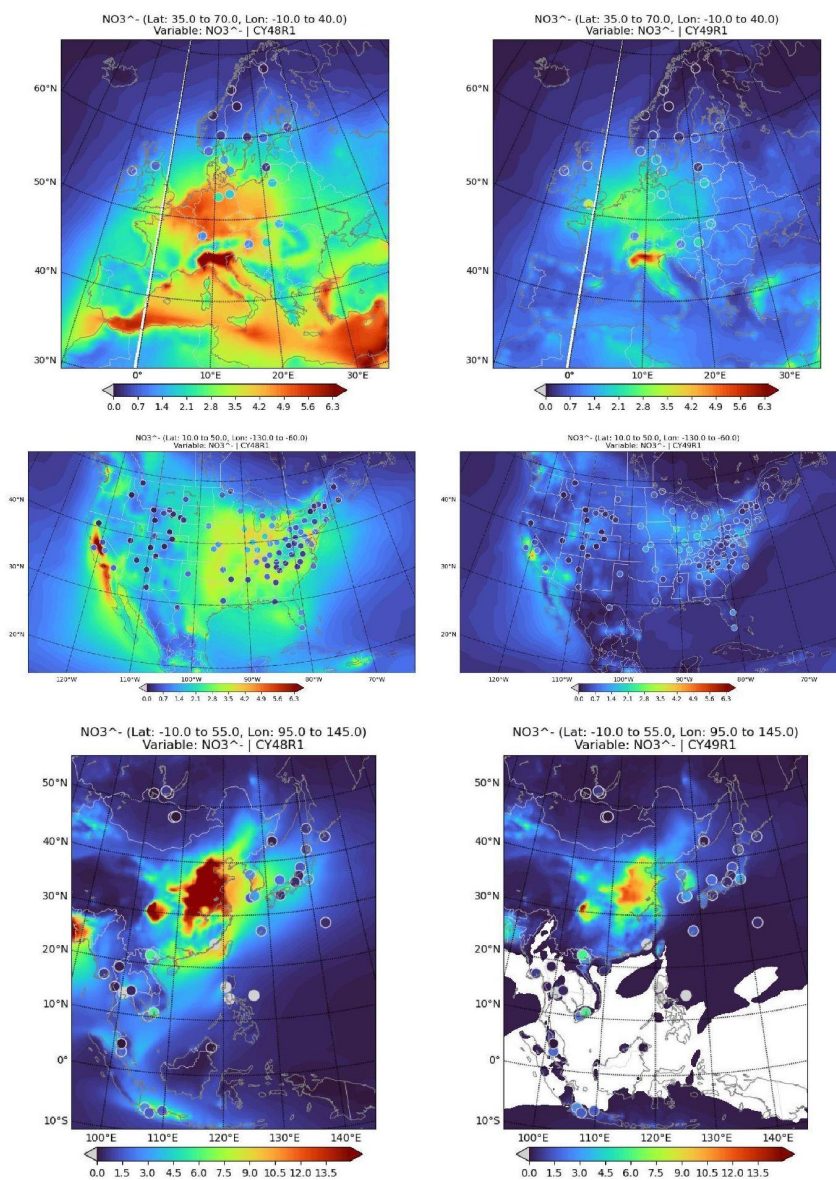
Figure 7: Annual mean comparisons of [NO₃⁻] simulated in CY48R1 and CY49R1, compared against measurements for the three selected regions, given in µg/m³. The corresponding regional statistics are provided in Table 8.

19

Geoscientific
Model Development
Discussions

619 **Table 8**: As for Table 2, but for NO_3^-.

NO_3^-	Europe (EMEP)		US (CASTNET)		SE Asia (EANET)	
	CY48R1	CY49R1	CY48R1	CY49R1	CY48R1	CY49R1
MB (ug/m³)	0.95	0.10 (-90%)	1.71	0.10 (-94%)	2.68	-0.16 (-94%)
RMSE	2.37	1.60 (-32%)	2.20	0.83 (-62%)	3.62	1.41 (-61%)
Pearsons R	0.41	0.58 (+29%)	0.31	0.57 (+46%)	0.65	0.52 (-20%)

620

621 In the U.S., a similar impact on $[NO_3^-]$ is observed as in Europe, where the high annual MB in $[NO_3^-]$
622 decreases significantly (94%) from CY48R1 to CY49R1. In CY48R1, $[NO_3^-]$ typically ranges from 2–4
623 µg/m³, with medium–range transport resulting in appreciable concentrations over the surrounding
624 oceans. Considering the precursors, there is surprisingly little variability in the observed annual mean
625 $[NO_3^-]$, despite the large difference in resident $[HNO_3(g)]$ across different states of the U.S., related to
626 the distribution of NO_x emissions (see Figure 5; Goldberg et al., 2021). Only in the southwest, around
627 California, are annual mean $[NO_3^-]$ values > 2.0 µg/m³, whereas typical annual mean $[NO_3^-]$ values
628 in CY49R1 are ≤ 1.0 µg/m³ for most of the U.S. This implies that the cations used as input for
629 EQSAM4Clim impose a limit on the phase transfer of $HNO_3(g)$ into more acidic aerosols through
630 neutralization of anions by cations in the particle phase.

631 **5. The changes in regional wet deposition**

632

633 In this section, we evaluate the temporal distribution and biases associated with the annual wet deposition of
634 soluble trace gas species and particulates. All three SIA species are lost to the surface via both dry and wet
635 deposition processes. Over the last few decades, the main source of acidification has shifted from SO_x-based to
636 NO_x-based, following the reduction measures for SO_x and increased emissions from sectors such as road transport.
637 Here, we assess whether the current version of IFS-COMPO captures the correct wet scavenging for the various
638 dissolved precursors and SIA. Evaluations are based on comparisons of model output against annual wet deposition
639 totals from observational networks. The concentrations of the dissolved precursors (i.e., $SO_2(aq)$, $NH_3(aq)$, and
640 $HNO_3(aq)$) also undergo wet deposition (in IFS-COMPO) and cannot be differentiated in the observational
641 networks, but are included in the measured totals. The wet deposition term is influenced by meteorological
642 parameters such as simulated large-scale and convective mixing, liquid and solid precipitation droplet size, SAD
643 (Surface Area Density), and the frequency and intensity of precipitation provided by the IFS model.

644 In Table 9, we present the changes in the global tropospheric burden, lifetime, and dry and wet deposition totals
645 for SO_4^{2-}, NH_4^+, and NO_3^- (fine and coarse) during 2018 across all simulations. The corresponding statistics for
646 the annual wet deposition means of SO_x, reduced N, and oxidized N are provided for the three selected global
647 regions in Table 10. The locations of the measurement sites are similar to those used for the SIA concentration
648 evaluations and have similar constraints with respect to representativity for the area. The stations' locations are
649 shown in the following figures, allowing for a direct comparison of the annual values without complications from
650 different sampling regimes regarding spatial representation.

651 **Table 9**: The global budget values for the burden, tropospheric lifetime, wet and dry deposition terms for SO_4^{2-},
652 NH_4^+, and NO_3^- in 2018. Totals are provided in Tg S/year and Tg N/year. Percentage difference changes are given
653 in parentheses.

	CY48R1	CY49R1_NOE4C	CY49R1
SO_4^{2-}			
Burden	0.4	0.6 (+30)	0.6 (+30)

	CY48R1	CY49R1_NOE4C	CY49R1
Lifetime (days)	3.4	4.4 (+29)	4.4 (+29)
Dry dep	5.8	5.4 (-7)	5.4 (-7)
Wet dep	43.1	43.9 (+2)	44.2 (+3)
NH_4^+			
Burden	0.3	0.4 (+32)	0.2 (-33)
Lifetime (days)	3.5	4.6 (+34)	4.1 (+18)
Dry dep	5.1	5.1 (-)	1.8 (-64)
Wet dep	27.5	27.1 (-2)	20.1 (-40)
NO_3^- (fine)			
Burden	0.01	0.01 (-)	0.02 (+86)
Lifetime (days)	4.9	5.4 (+12)	6.1 (+25)
Dry dep	0.2	0.2 (-21)	0.1 (-32)
Wet dep	0.6	0.5 (-13)	1.0 (+64)
NO_3^- (coarse)			
Burden	0.01	0.01 (-)	0.01 (-)
Lifetime (days)	3.4	3.8 (+11)	2.4 (-29)
Dry dep	1.5	2.5 (+73)	1.2 (-18)
Wet dep	3.5	2.8 (-20)	0.7 (-79)

654

655 **Table 10**: The annual MB, RMSE, and Pearson's R values for the comparisons of weekly mean regional wet
656 deposition totals of dissolved $SO_2 + SO_4^{2-}$, $NH_3 + NH_4^+$, and $HNO_3 + NO_3^-$, compared against composites
657 assembled from the regional observation networks for 2018 shown in Figures 8-10 for Europe, the U.S., and
658 Southeast Asia. Percentage difference changes are calculated as $((CY49R1 - CY48R1)/CY48R1) * 100$.

	Europe (EMEP)		US (CASTNET)		SE Asia (EANET)	
SO_X	CY48R1	CY49R1	CY48R1	CY49R1	CY48R1	CY49R1
MB (mgS/m²/yr)	-42	-38 (-9)	137	190 (+39)	-44.2	8.7 (-80)
RMSE	88.2	85 (-3)	203	270 (+33)	447	500.3 (+12)
Pearsons R	0.55	0.58 (+6)	0.68	0.66 (-3)	0.72	0.65 (-10)
Reduced N						
MB (mgN/m²/yr)	61	25.9 (-58)	8.4	6.8 (-21)	12	-44 (+260)
RMSE	114	93.4 (-18)	76.0	81.3 (+7)	318	302 (-5)
Pearsons R	0.69	0.68 (-1.4)	0.77	0.72 (-16)	0.75	0.71 (-1)
Oxidised N						
MB (mgN/m²/yr)	9.7	-1.4 (-86)	130	99.7 (-23)	142	98.3 (-31)
RMSE	69	72 (+4)	153	122.6 (-20)	324	274.3 (-15)
Pearsons R	0.50	0.47 (-6)	0.86	0.85 (-1)	0.67	0.68 (+2)

659

660

21

661

662

5.1 Total annual wet S deposition

663

664 Figure 11 shows the regional distribution of annual wet S deposition for Europe, the U.S., and Southeast Asia in
665 both CY48R1 and CY49R1 during 2018. To allow direct comparison across regions, we use a color scale covering
666 values up to 1000 mg S/m²/year. The global budget terms for SO_4^{2-} are presented in Table 9, showing that despite
667 the global burden increasing by one third, only small increases of a few percent occur in the annual wet SO_4^{2-}
668 totals (Rémy et al., 2024). However, the significant increase in the tropospheric SO_4^{2-} lifetime means that more
669 remains in the aerosol phase, impacting the degree of scattering in IFS-COMPO, as shown in AOD comparisons
670 in Rémy et al. (2024). The most significant change is in the direct gas-phase production of $H_2SO_4(g)$, where
671 increases in $[SO_2(g)]$ subsequently increase the total mass scavenged into aqueous cloud droplets. This results in
672 some acidification (slowing in-situ oxidation, cf. Table 3), buffered somewhat by increased phase transfer of
673 $NH_3(g)$ (cf. Table 5). Although there is a 15% reduction in global $SO_2(aq)$ wet deposition, increases in $[SO_4^{2-}(aq)]$
674 result in an increase in the cumulative wet S deposition totals.

675 In Europe, the changes between model simulations are similar to those for $SO_2(g)$ and SO_4^{2-} particle concentrations
676 discussed in Section 4. Compared to the annual EMEP observational mean values, which range from 100-900 mg
677 S/m²/year, CY48R1 generally underestimates values by approximately 100-150 mg S/m²/year in northwest
678 Europe, Poland, and the Iberian Peninsula. In other regions, agreement is good, capturing the observed deposition
679 gradient from Germany into Austria and northern Italy. A limited number of measurement stations exhibit very
680 high localized values (e.g., southwest Ireland, Palma), indicating missing primary emission sources in the global
681 inventory. In CY49R1, strong similarities are observed for Benelux, Denmark, and Italy, with negative biases of
682 around 50-100 mg S/m²/year. A significant negative annual MB exists in Europe, decreasing by around 10 mg
683 S/m²/year in CY49R1 (cf. Table 10), with a marginal increase in correlation. This is influenced by the associated
684 negative MB for $SO_2(g)$ during summer (cf. Figure 1) and the large values observed at selected stations influencing
685 the regional mean.

686 In the U.S., there is a stark contrast to Europe. CASTNET annual mean values show an observational gradient in
687 wet deposition totals, similar to the primary SO_2 emission sources (cf. Figure A1 in the Appendix), with maximum
688 values reaching 300-400 mg S/m²/year toward the East Coast. CY48R1 captures this gradient well but with large
689 positive biases of >100 mg S/m²/year, resulting in maximum values of 700-900 mg S/m²/year. Significant annual
690 wet deposition occurs in the Atlantic (250-300 mg S/m²/year) due to the oxidation of DMS (released from the
691 ocean) and long-range transport of $SO_2(g)/SO_4^{2-}$ from anthropogenic source regions. In CY49R1, the area of
692 maximum wet S deposition increases around regions like New York State, resulting in a 40% increase in positive
693 annual MB to 190 mg S/m²/year. This contrasts with the significant improvement in the annual MB for $[SO_4^{2-}]$, as
694 shown in Table 7, indicating an increase in scavenging into the aqueous phase of SO_4^{2-} particles due to other
695 cumulative updates in IFS-COMPO (cf. Table 9), partly due to a 10% increase in gas-phase SO_2 to H_2SO_4 (cf.
696 Table 9).

697 In Southeast Asia, EANET annual wet deposition totals show that more than double the amount of S deposition
698 occurs compared to Europe or the U.S., reaching 1200-1300 mg S/m²/year in central China and Indonesia. The
699 temporal distribution of stations shows a positive gradient between deposition totals in China and those extending
700 toward Indonesia (2000-2200 mg S/m²/year, not shown). This highlights the importance of SO_4^{2-} transport,
701 considering the low regional $SO_2(g)$ precursor mixing ratios near the equator (cf. Figure A1 in the Appendix), with
702 primary sources being infrequent volcanic eruptions that typically inject SO_2 above the boundary layer (thus with
703 limited surface impact).

704 Along the eastern coast of China, observations show annual totals of 250-350 mg S/m²/year, contrasting with
705 higher values in central China. This is surprising, considering that high SO_2 emissions are defined in IFS-COMPO
706 around South Korea rather than central China. This implies that the regional SO_2 emissions employed for this
707 region may be overestimated, given the low regional deposition values. The regional annual MB improves
708 markedly to 8.7 mg S/m²/year, which is very low given the high values in the measurements. However, the
709 correlation coefficient degrades from 0.72 to 0.65.

710
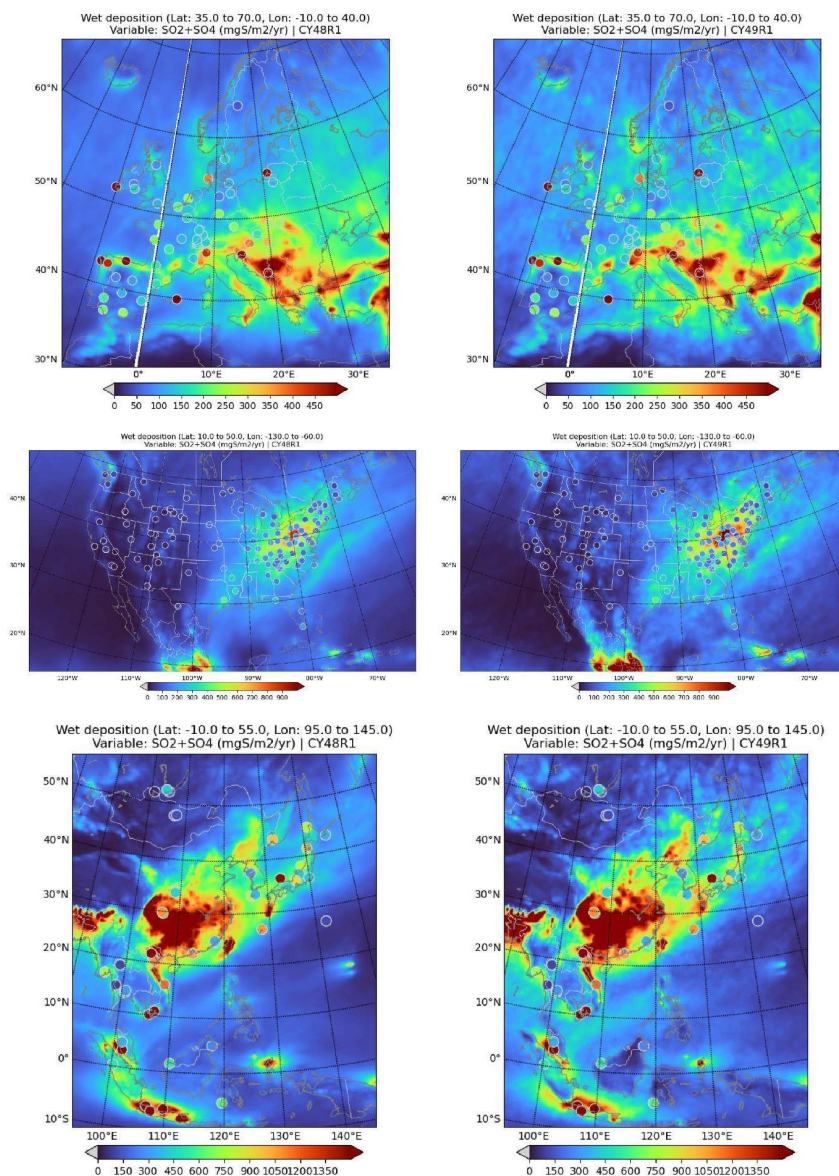
Figure 8: Annual comparisons of the cumulative wet deposition totals of dissolved SO₂ and SO₄²⁻ aerosol (mg S/m²/year) for 2018, simulated in CY48R1 (left column) and CY49R1 (right column), shown for Europe (top), the U.S. (middle), and Southeast Asia (bottom). The corresponding statistics are provided in Table 9.
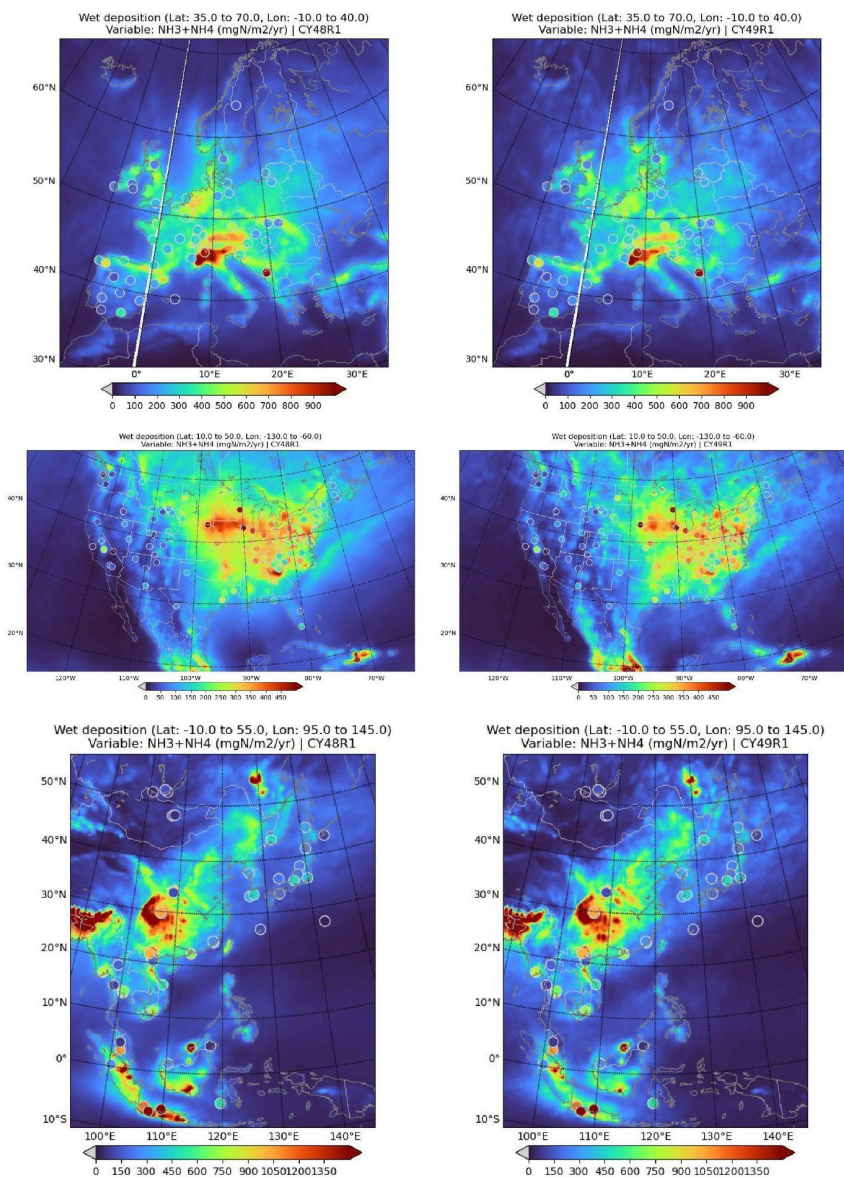
23

5.2 Total annual wet NH_x deposition

Figure 9 shows the corresponding changes in total annual mean wet deposition of reduced N for both CY48R1 and CY49R1 during 2018. The sampling stations are the same as those used for the wet S deposition evaluation. In Table 9, the global chemical budget terms for NH_4^+ show that cumulative updates to IFS-COMPO increase the tropospheric burden by one third (similar to SO_4^{2-}, as $(NH_4)_2SO_4$ is a dominant SIA species, Seinfeld and Pandis, 2006). However, this is reversed when applying EQSAM4Clim for aerosol and cloud pH, as shown when comparing CY48R1 and CY49R1. This results in significant decreases in both global dry and wet deposition totals (>50%, cf. Table 9) across the three regions.

In Europe, where high summertime $NH_3(g)$ mixing ratios are simulated (cf. Figure 4 in Section 4), EMEP observational annual wet deposition totals show peak values in the Balkans and northern Italy (Po Valley), with regional variability in France (250-350 mg N/m²/year). In regions with low NH_3 emissions, such as Scandinavia and the Iberian Peninsula, wet deposition totals range from 50-200 mg N/m²/year. In CY48R1, high surface $NH_3(g)$ mixing ratios (5-15 ppb; see Figure A3 in the Appendix) result in relatively high NH_x annual wet deposition totals of 350-500 mg N/m²/year for northwest and central Europe (e.g., Benelux, Austria). Measured annual mean values are typically exceeded, resulting in an annual MB of 61 mg N/m²/year, albeit with a high correlation (0.69, cf. Table 9). The continental distribution is well represented, though high values extend too far east and west of Europe. In CY49R1, the area with maximum values (>450 mg N/m²/year) shrinks. The reduction in $[NH_4^+]$ (cf. Table 5) decreases the annual MB in wet deposition by nearly 60%, without degrading the correlation coefficient. The application of EQSAM4Clim significantly improves the simulation of reduced N wet deposition in IFS-COMPO for Europe.

In the U.S., CASTNET observations show a similar east-west gradient in total reduced N wet deposition as seen in $NH_3(g)$ surface mixing ratios and $[NH_4^+]$ distributions (cf. Figure A3 and Figure 9, respectively). Observed wet deposition values range from 30-400 mg N/m²/year, indicating that deposition levels are lower where local NH_3 emission sources are absent (lower than in Europe). In CY48R1, the continental gradient is captured, though maximum values in Iowa are not observed in the measurements (>100% MB), influenced by high local NH_3 emission flux (cf. Figure A3). On the East Coast, where most NH_3 sources are located, CY48R1 generally overestimates wet deposition. Compared to Europe, the annual MB for the U.S. is low (9 mg N/m²/year), reflecting large positive biases on the East Coast, moderated by underestimates elsewhere. A high correlation (R=0.77) is achieved in CY49R1. Although NH_4^+'s spatial distribution remains similar between cycles, the reduction in $[NH_4^+]$ reduces the annual MB by 21%, with a slight degradation in correlation.

In Southeast Asia, EANET observational annual wet deposition totals are higher than in Europe and the U.S., ranging from 200-2400 mg N/m²/year (not shown), with the highest values in Indonesia and Vietnam. The simulated temporal distribution of reduced N wet deposition captures the variability across individual stations well across a wide area. In CY48R1, the annual MB is 12 mg N/m²/year on high annual totals, making it the lowest MB among the regions, with a high correlation (0.75). In CY49R1, there is a larger negative MB (though still relatively small compared to the large totals), despite the lower positive MB simulated for $[NH_4^+]$ compared to CY48R1 (cf. Table 6).

Figure 9: Annual comparisons of the cumulative wet deposition totals of dissolved NH$_3$ and NH$_4^+$ aerosol (mg N/m²/year) for 2018, simulated in CY48R1 (left column) and CY49R1 (right column), shown for Europe (top), the U.S. (middle), and Southeast Asia (bottom). The corresponding statistics are provided in Table 9.

5.3 Total annual wet NOₓ deposition

Finally, Figure 10 shows the corresponding changes in total annual mean wet deposition of oxidized N for both CY48R1 and CY49R1 during 2018. The global chemical budget terms provided in Table 7 show an increase in the gas-phase production term for HNO_3, with a relatively constant heterogeneous conversion term for N_2O_5 when summed over various reactive surfaces. Once formed, a significant fraction of HNO_3 is directly scavenged into aqueous cloud droplets and deposited as wet (acidic) deposition (cf. Rémy et al., 2024). However, the large biases in $HNO_3(g)$ reveal a limit to the wet scavenging term, leaving an excess in the gas phase, impacting the results in this section. Note that particulate NO_3^- takes various chemical forms in IFS-COMPO ($Ca(NO_3)_2$, $NaNO_3$, NH_4NO_3), so there is only partial commonality between changes in NH_4^+ and NO_3^-. Applying EQSAM4Clim reduces NH_4^+ concentrations and burdens, while $HNO_3(g)$ concentrations increase (cf. Table 5 and Figure 6).

In Europe, EMEP observational annual wet deposition totals of oxidized N range from 150-275 mg N/m²/year, correlating with the homogeneous distribution of $[NO_3^-]$ (see Section 4.3). A few high outliers are likely influenced by strong local NOₓ emissions. Although modest differences in cumulative wet deposition of $[NO_3^-]$ occur between CY48R1 and CY49R1, the regional bias in oxidized N wet deposition improves markedly, decreasing by 80% (from positive to negative), though no significant improvement in the (time-sensitive) correlation is observed.

In the U.S., higher values of oxidized N deposition occur on the East Coast, driven by NOₓ emissions (see Figure 13). CASTNET observational wet deposition values range from 50-500 mg N/m²/year, showing a strong longitudinal gradient. This gradient is captured well, though CY48R1 typically overestimates by 100-200 mg N/m²/year, e.g., in New York State and surrounding regions. In the western U.S., observations show values between 0-100 mg N/m²/year, with positive model biases of 100 mg N/m²/year in the northwest states in both versions. In the southern U.S., CY48R1 overestimates by 50-70 mg N/m²/year, which decreases significantly in CY49R1. CY48R1 exhibits a large positive bias of 130 mg N/m²/year, improved by 23% in CY49R1. Again, Pearson's R remains relatively unaffected, indicating the governing influence of the spatial distribution of main point sources and limited impact on forecasts (as IFS-COMPO is not employed here as a fully coupled forecasting system).

In Southeast Asia, EANET observational total wet deposition values range from 50-800 mg N/m²/year, with the highest values (>2000 mg N/m²/year) occurring on the Malaysian coast. In northern China, wet deposition totals of up to 400 mg N/m²/year occur, approximately half of what is observed near the southern coast and eastward. The highest simulated wet deposition totals occur in southwest China, correlating with high NOₓ emissions. Comparing CY48R1 and CY49R1 shows a marked 31% decrease between cycles, again with limited changes to the correlation.
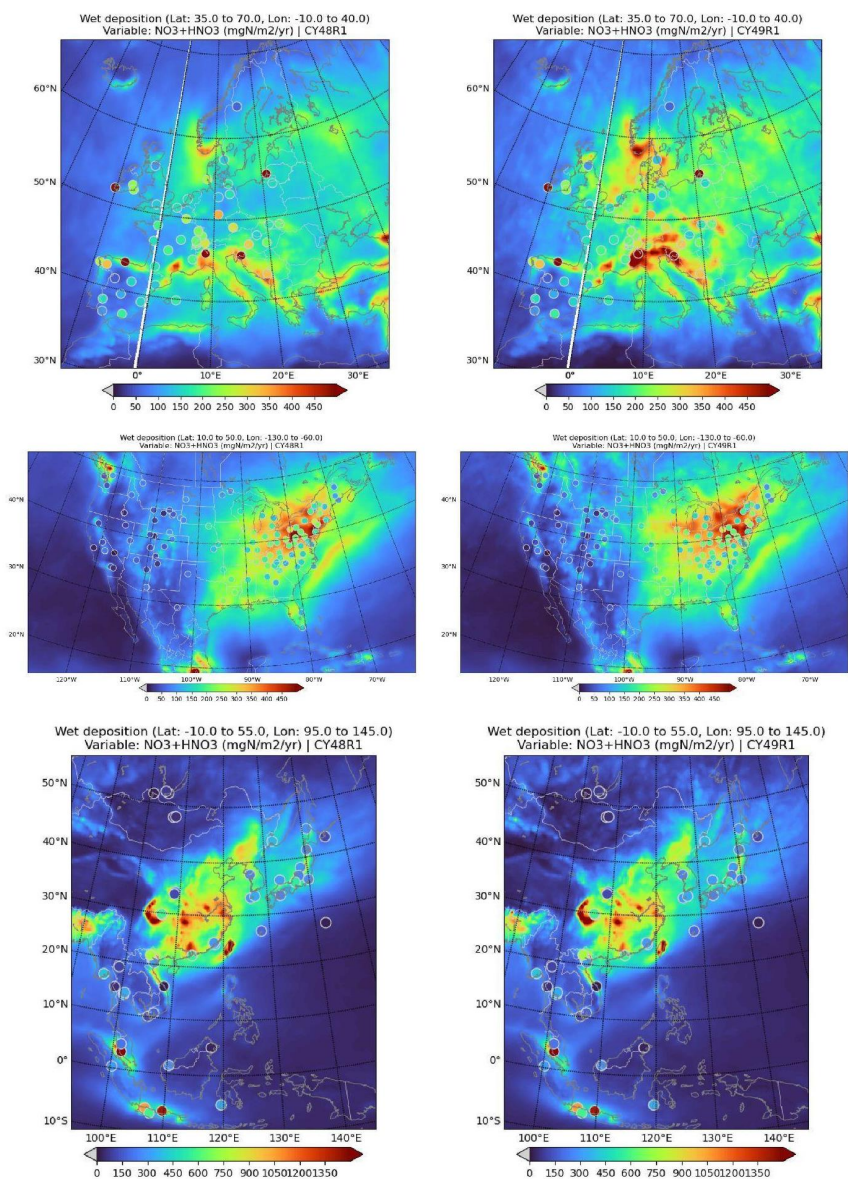
Figure 10: Annual comparisons of the cumulative wet deposition totals of dissolved HNO_3 and NO_3^- aerosol (mg N/m²/year) for 2018, simulated in CY48R1 (left column) and CY49R1 (right column), shown for Europe (top), the U.S. (middle), and Southeast Asia (bottom). The corresponding statistics are provided in Table 9.

6 Conclusions

In this paper, we build on previous evaluations of IFS-COMPO CY49R1 performance presented in Rémy et al. (2024), which assessed the impact of EQSAM4Clim and its revised calculation of aerosol and cloud pH (Metzger et al., 2024) on improving air quality forecasts by segregating and investigating individual inorganic components. To scrutinize its effect on atmospheric composition, we compared the current operational IFS version, which contains a basic description of aerosol and cloud pH (CY48R1), with the next operational IFS version (CY49R1),

27

807 which uses EQSAM4Clim in combination with a unified wet scavenging approach and other developments.
808 Further improvements were also made to both in-cloud and below-cloud scavenging of soluble trace gases and
809 aerosols through updated parameterizations, as detailed in Rémy et al. (2024).

810 We have shown that the most significant impacts of the IFS-COMPO updates are related to the production efficacy
811 of SIA and the subsequent phase partitioning of reduced/oxidized nitrogen species. Comparing simulations with
812 and without EQSAM4Clim reveals that changes in SIA are primarily caused by alterations in gas/aerosol
813 partitioning. The verification and analysis are shown for three dominant source regions—Europe, the U.S., and
814 Southeast Asia—by focusing on surface concentration and wet deposition observations for 2018, compared against
815 observational composites. Most of the simulated SIA surface concentration and wet deposition fields are improved
816 by the proposed CY49R1 changes, particularly by the use of EQSAM4Clim.

817 For $SO_2(g)/SO_4^{2-}$, only moderate changes occur in the conversion rate. For $SO_2(g)$, a 7% increase in the global
818 tropospheric burden indicates less phase transfer due to limitations in uptake caused by the increase in solution
819 pH. An increase in the gas-phase production of $H_2SO_4(g)$, which is subsequently scavenged, offsets a modest
820 reduction in the aqueous-phase production term. For surface $[SO_2(g)]$, this results in a lower mean annual bias for
821 Europe with moderate correlation, while a higher negative bias with little correlation is observed for the U.S. In
822 China, no appreciable impact occurs, as a high positive bias of 11.5 µg/m³ is observed with respect to CNEC and
823 a near-zero correlation coefficient. For $[SO_4^{2-}]$, the tropospheric burden and lifetime increase by one third due to
824 the IFS-COMPO updates, leading to a reduction in the annual mean biases for Europe and the U.S., along with
825 increases in the corresponding correlation coefficients. However, in China, performance degrades, with a positive
826 annual mean bias and a decrease in the correlation coefficient.

827 For $NH_3(g)/NH_4^+$, the changes are more substantial, resulting in beneficial improvements in global modeling of
828 reduced nitrogen. For $NH_3(g)$, the tropospheric burden nearly doubles due to a halving of the conversion rate into
829 NH_4^+, with more $NH_3(g)$ being directly deposited to the surface. For surface $[NH_3(g)]$, there is a contrasting change
830 in the simulated weekly mean bias between Europe and the U.S. In Europe, there is no significant improvement in
831 the persistent high weekly mean biases, which increase by 10-25% during spring and summer despite all updates.
832 In the U.S., the lower weekly $[NH_3(g)]$ results in an associated low bias in the simulations, meaning the increase
833 in the tropospheric burden improves surface comparison markedly. For $[NH_4^+]$ in Europe, EQSAM4Clim's
834 application results in limited changes in the simulated weekly bias during winter, while significant reductions are
835 observed in summer, with an associated increase in the annual mean correlation. In the U.S. and China, similar
836 reductions in the annual mean bias of nearly 50% occur, although the correlation is slightly reduced.

837 For $HNO_3(g)/NO_3^-$, the changes are similar to those for $NH_3(g)/NH_4^+$ partitioning due to the speciation of SIA,
838 which is mainly linked via NH_4NO_3. Gas-phase production of $HNO_3(g)$ increases without an associated increase
839 in the global tropospheric burden, due to increased loss to the surface via dry deposition. EQSAM4Clim increases
840 the fine aerosol component while reducing the coarse aerosol component, which decreases the fraction of $HNO_3(g)$
841 held in the particulate phase by 50%. In Europe and the U.S., persistent negative biases for $HNO_3(g)$ are changed
842 to significant positive biases. For $[NO_3^-]$, significant improvements in annual mean biases occur globally, as
843 illustrated by the three chosen regions, along with improvements in simulated correlation coefficients.

844 For the wet deposition component, changes in SIA concentrations are qualitatively similar to the annual wet
845 deposition totals, although regional changes are variable and species-specific. In Europe, reductions are observed
846 in the simulated annual mean bias for all three chemical types, with oxidized N improving markedly. In the U.S.,
847 the annual mean bias increases for wet S deposition, while biases for both reduced and oxidized wet N decrease.
848 In Southeast Asia, there is a marked improvement in wet S deposition, a moderate improvement in oxidized wet
849 N, and a degradation in reduced wet N. Overall, the recent improvements brought by EQSAM4Clim (Metzger et
850 al., 2024), as applied here and in Rémy et al. (2024), show that CY49R1 is fit for purpose in capturing regional
851 particle concentration and loss terms via wet deposition.

852   **Appendix**

853
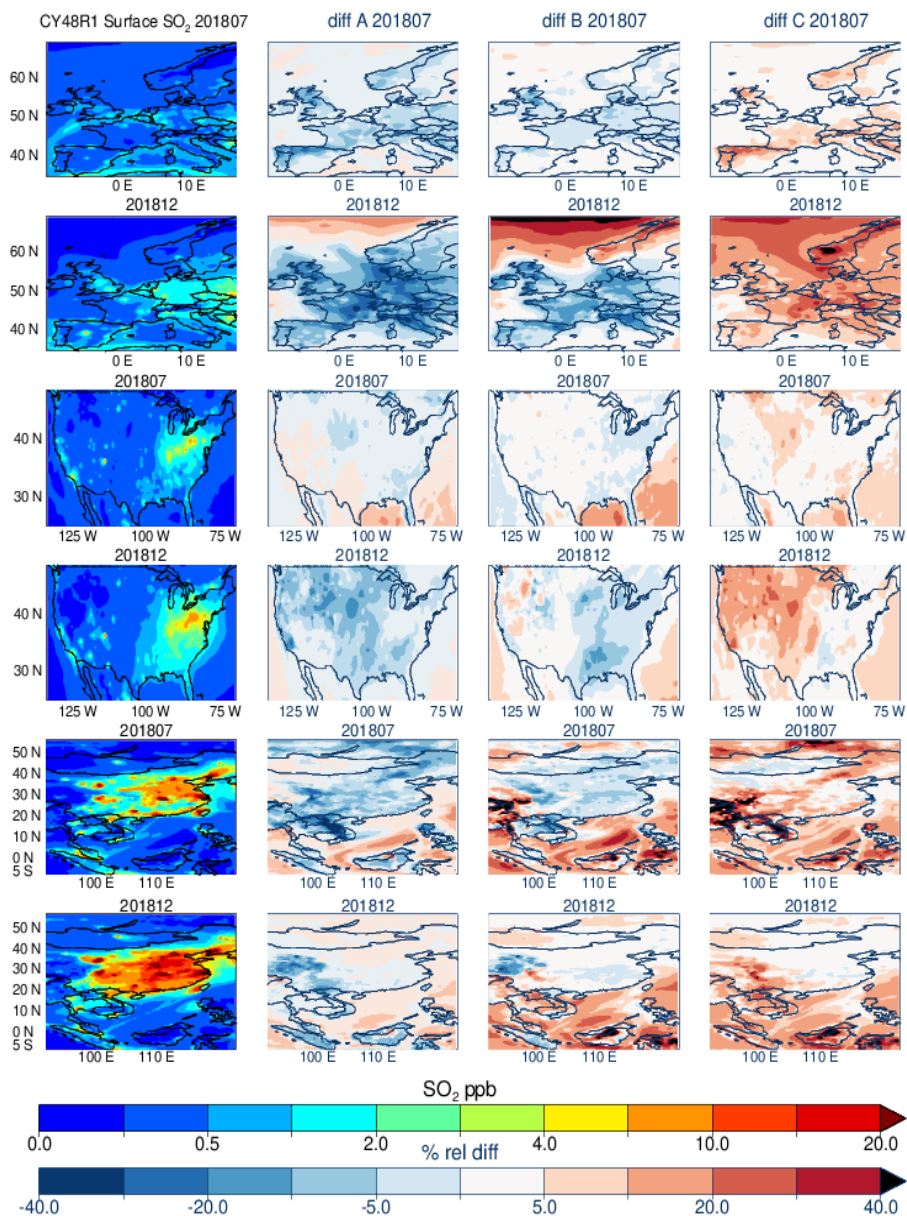
Figure A1: The horizontal seasonal mean distribution for surface SO_2 for CY48R1 for July and December 2018 for Europe (top), the United States (middle), and Southeast Asia (bottom). The corresponding relative differences are compared against the other simulations. Panel definitions: Diff A = (CY49R1_NOE4C - CY48R1)/CY48R1; Diff B = (CY49R1 - CY48R1)/CY48R1; and Diff C = (CY49R1 - CY49R1_NOE4C)/CY48R1.
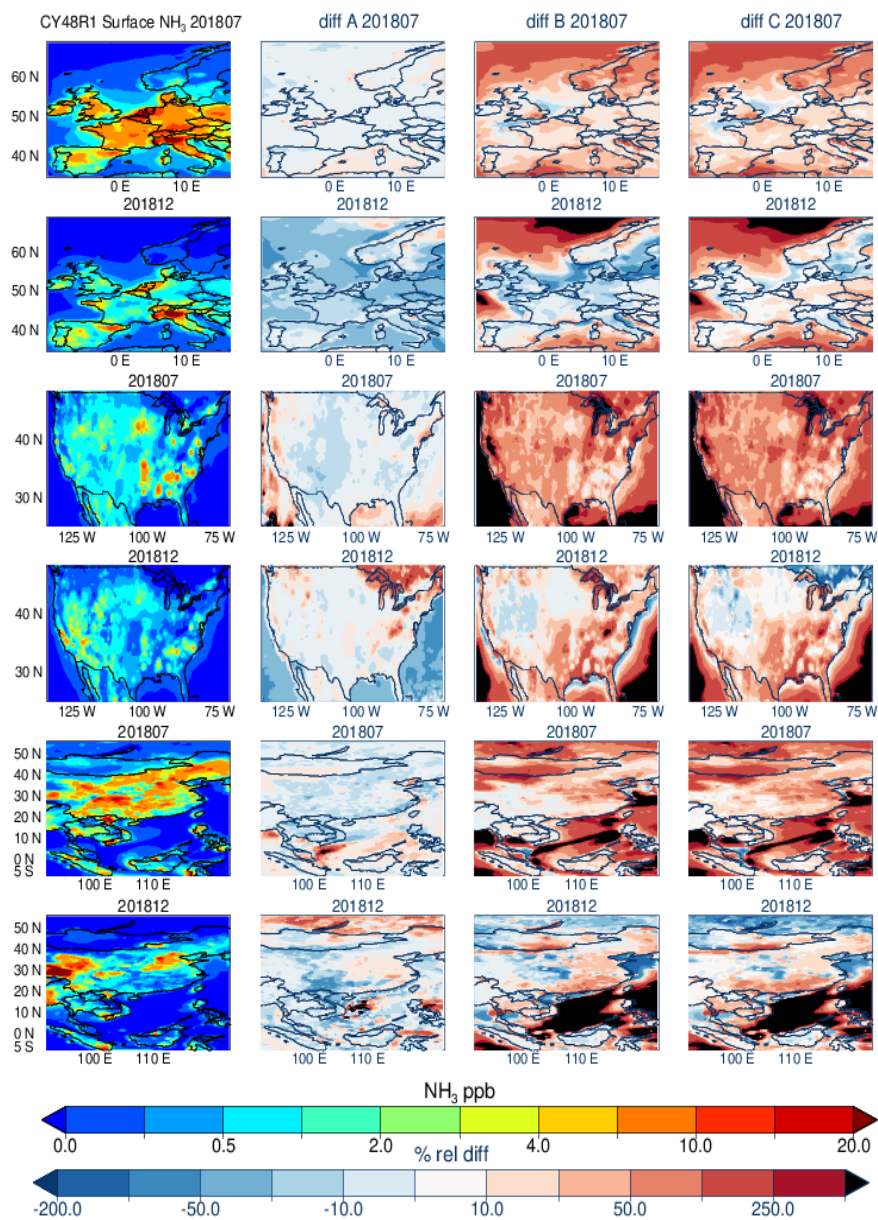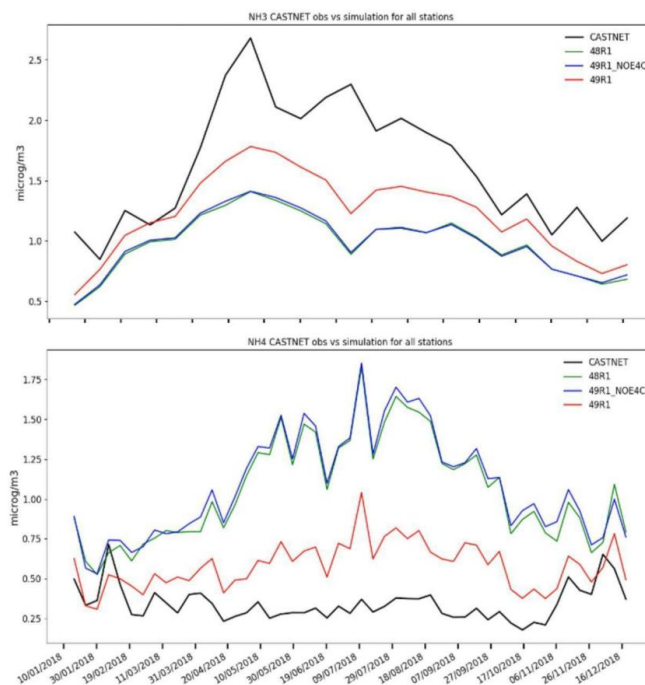
858

29
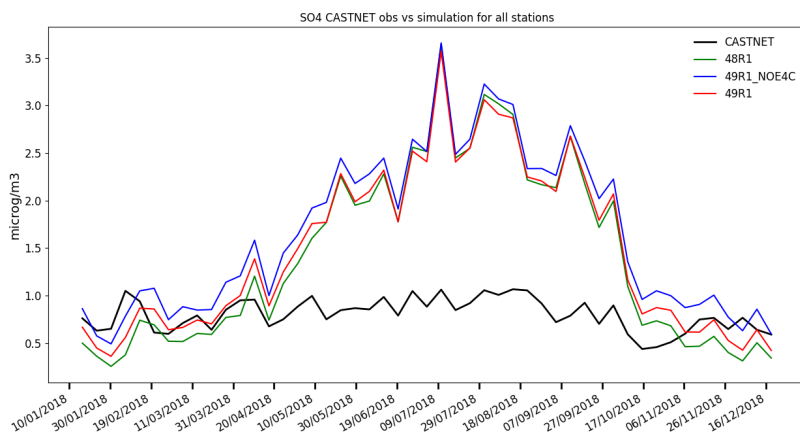
Figure A2: Comparisons of weekly SO_4^{2-} concentrations (µg/m³) in the U.S. between CASTNET composites and the IFS-COMPO simulations CY48R1, CY49R1_NOE4C, and CY49R1 for 2018.

Figure A3: As for Figure A1, except for NH₃. Panel definitions: Diff A = (CY49R1_NOE4C - CY48R1)/CY48R1; Diff B = (CY49R1 - CY48R1)/CY48R1; and Diff C = (CY49R1 - CY49R1_NOE4C)/CY48R1.

Figure A4 : Comparisons of weekly NH₃ and NH₄⁺ concentrations (µg/m³) in the U.S. between CASTNET composites and the IFS-COMPO simulations CY48R1, CY49R1_NOE4C, and CY49R1 for 2018.
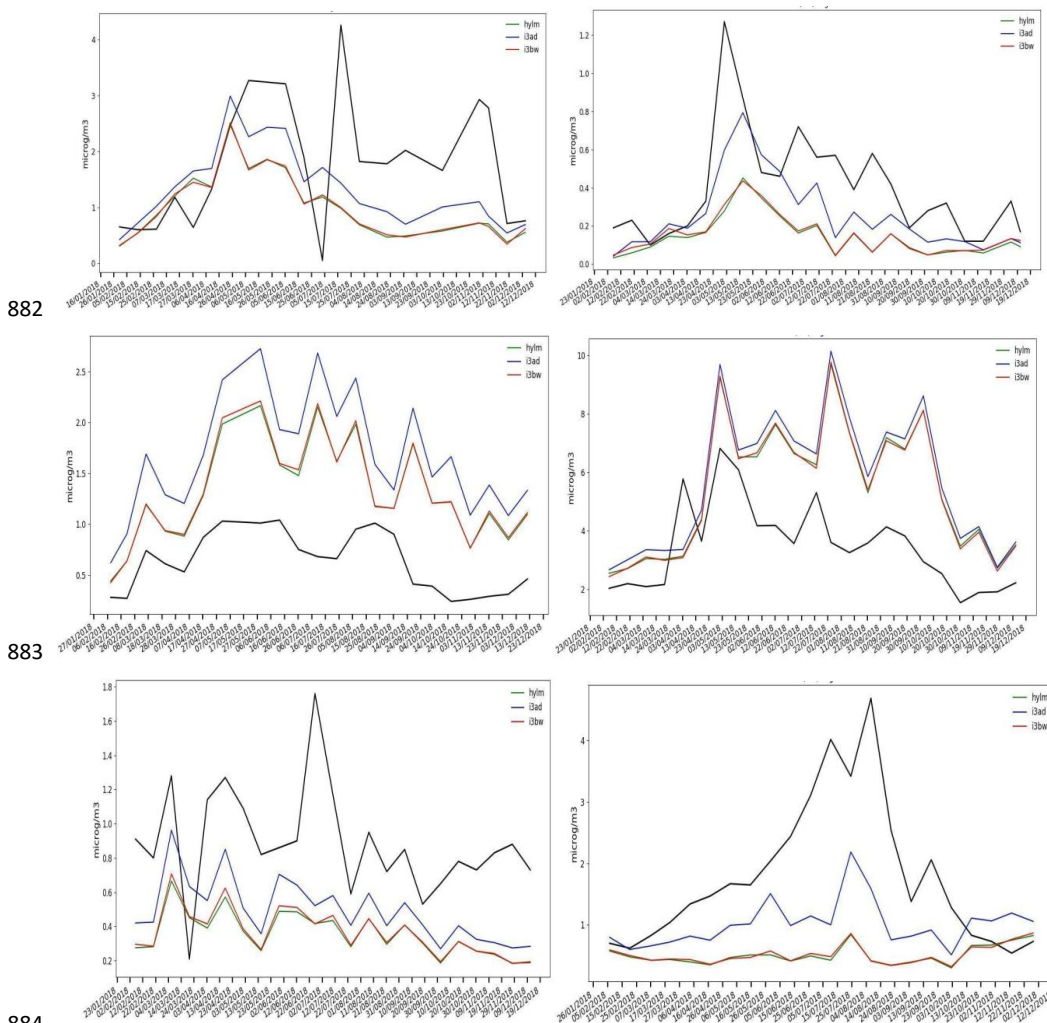
32

Geoscientific
Model Development
Discussions
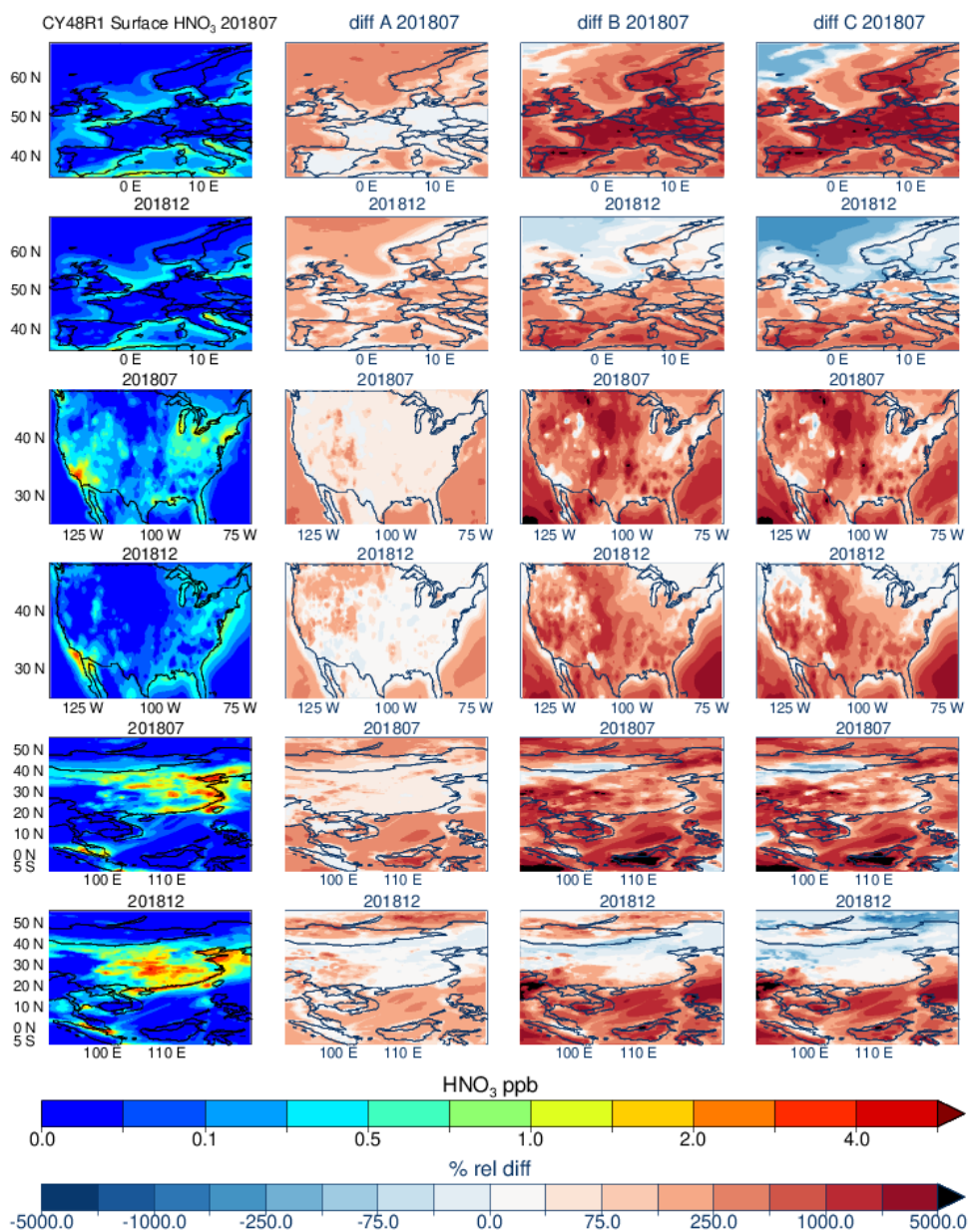

Figure A5: Comparisons of weekly mean NH_3 concentrations (µg/m³) from CY48R1, CY49R1_NOE4C, and CY49R1 against measurements from selected stations participating in the AMoN network for 2018. From top left to bottom right, station ID OH09 (Oxford, Ohio, 39.53°N, 84.72°W), NY98 (Whiteface Mountain, New York State, 44.39°N, 73.85°W), AR03 (Caddo Valley, Arizona, 34.17°N, 93.10°W), AL99 (Sand Mountain, Alabama, 34.29°N, 86.0°W), CA67 (Joshua Tree National Park, California, 34.1°N, 116.39°W), and FL19 (Indian River, Florida, 27.85°N, 80.45°W).

Table A1: Statistics for the regional distribution of gaseous NH_3 in the U.S. compared against a composite of measurements from all 18 stations participating in the AMoN measurement network for 2018. Relative percentage differences are included as (CY49R1 - CY48R1)/CY48R1.
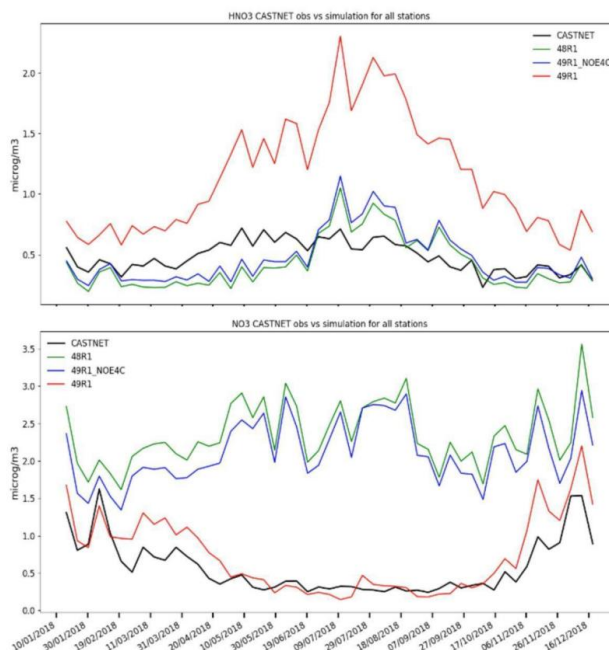
Diagnostics	CY48R1	CY49R1_NOE4C	CY49R1
MB (µg/m³)	-0.50	-0.49 (+2.0)	-0.26 (+48.0)
RMSE	1.79	1.79 (-)	1.71 (+4.4)
Pearsons R	0.49	0.49 (-)	0.52 (+6.1)

33

Figure A6: As for Figure 1, except for HNO₃. Panel definitions: Diff A = (CY49R1_NOE4C - CY48R1)/CY48R1; Diff B = (CY49R1 - CY48R1)/CY48R1; and Diff C = (CY49R1 - CY49R1_NOE4C)/CY48R1.

Geoscientific
Model Development
Discussions

899

Figure A7: Comparisons of weekly HNO_3 and NO_3^- concentrations ($\mu g/m^3$) in the U.S. between CASTNET composites and the IFS-COMPO simulations CY48R1, CY49R1_NOE4C, and CY49R1 for 2018.

Author Contributions

JEW and SM were the principal authors of the paper and produced most of the figures. SR conducted the IFS-COMPO simulations and performed the regional comparisons made against observational datasets for evaluating the deposition fluxes. SM provided and integrated EQSAM4Clim for the more accurate calculation of pH in aerosols and clouds. VH updated the model towards CY49R1 and handled technical updates with respect to the implementation of EQSAM4Clim. JF is a representative of the CAMS consortium under which this work was conducted.

Code and Data Availability

Model codes developed at ECMWF are the intellectual property of ECMWF and its member states and are therefore not publicly available. ECMWF member-state weather services and their approved partners may be granted access. Access to a version of IFS (OpenIFS) that includes this experimental cycle may be obtained from ECMWF under an OpenIFS license. More details can be found at https://confluence.ecmwf.int/display/OIFS/About+OpenIFS. The surface data for IFS-COMPO used for this study is available on Zenodo (https://doi.org/10.5281/zenodo.13902673).

Competing Interests

At least one of the co-authors is a member of the editorial board of Geoscientific Model Development.

Acknowledgements

924

925   References
926

927   van der A, R. J., Ding, J., and Eskes, H.: Monitoring European anthropogenic NO_x emissions from space, Atmos.
928   Chem. Phys., 24, 7523–7534, https://doi.org/10.5194/acp-24-7523-2024 , 2024.

929   Aas, W., Mortier, A., Bowersox, V. *et al.* Global and regional trends of atmospheric sulfur. *Sci Rep* 9, 953,
930   https://doi.org/10.1038/s41598-018-37304-0, 2019.
931

932   Aas, W., Fagerli, H., Alastuey, A., Cavalli, F., Degorska, A., Feigenspan, S., Brenna, H., Gliß, J., Heinesen, D.,
933   Hueglin, C., Holubová, A., Jaffrezo, J.L., Mortier, A., Murovec, M., Putaud, J.P., Rüdiger, J., Simpson, D.,
934   Solberg, S., Tsyro, S., Tørseth, K. and Yttri, K.E. : Trends in Air Pollution in Europe, 2000–2019. Aerosol Air
935   Qual. Res. 24, 230237. https://doi.org/10.4209/aaqr.230237, 2024.
936

937   Ault, A.P : Aerosol Acidity: Novel Measurements and Implications for Atmospheric Chemistry, *Acc. Chem. Res,*
938   53, 9, 1703–1714, https://doi.org/10.1021/acs.accounts.0c00303, 2020.

939   Benish, S. E., Bash, J. O., Foley, K. M., Appel, K. W., Hogrefe, C., Gilliam, R., and Pouliot, G.: Long-term
940   regional trends of nitrogen and sulfur deposition in the United States from 2002 to 2017, Atmos. Chem. Phys., 22,
941   12749–12767, https://doi.org/10.5194/acp-22-12749-2022, 2022.

942   Chang, C.-T., Wang, L., Wang L-J, Liu, C-P, Yang, C-J, Huang, J-C., Wang, C-P, Lin N-H. and Lin, T-C.: On the
943   seasonality of long-range transport of acidic pollutants in East Asia, Environ.Res.Letts., 17(9), doi:10.1088/1748-
944   9326/ac8b99, 2022.

945   Chen J, Cheng M, Krol M, de Vries W, Zhu Q, Liu X, Zhang F and Xu W (2023), Trends in anthropogenic
946   ammonia emissions in China since 1980: A review of approaches and estimations. Front. Environ. Sci.
947   11:1133753, doi: 10.3389/fenvs.2023.1133753.

948   Croft, B., Lohmann, U., Martin, R. V., Stier, P., Wurzler, S., Feichter, J., Posselt, R., and Ferrachat, S.: Aerosol
949   size-dependent below-cloud scavenging by rain and snow in the ECHAM5-HAM, Atmos. Chem. Phys., 9, 4653–
950   4675, 2009.

951   de Bruine, M., Krol, M., van Noije, T., Le Sager, P., and Rockmann, T.: The impact of precipitation evaporation
952   on the atmospheric aerosol distribution in EC-Earth v3.2.0, Geosci. Model Dev., 11, 1443–1465, 2018.

953   Dentener, F., Drevet, J., Lamarque, J. F.,Bey, I., Eickhout, B., Fiore, A. M., Hauglustaine, D., Horowitz, L. W.,
954   Krol, M.,Kulshrestha, U. C., Lawrence, M., Galy-Lacaux, C., Rast, S., Shindell, D., Stevenson, D., Van Noije, T.,
955   Atherton, C., Bell, N., Bergman, D., Butler, T., Cofala, J., Collins, B., Doherty, R., Ellingsen, K., Galloway, J.,
956   Gauss, M., Montanaro, V., Muller, J. F., Pitari, G., Rodriguez, J.,Sand erson, M., Solmon, F., Strahan, S., Schultz,
957   M., Sudo, K., Szopa, S., and Wild, O.: Nitrogen and sulfur deposition on regional and global scales:A multimodel
958   evaluation, Global Biogeo. Cycles, 20, GB4003, doi:10.1029/2005GB002672, 2006.

959   Deschaseaux, E., O'Brien, J., Siboni, N., Petrou, K., and Seymour, J. R.: Shifts in dimethylated sulfur
960   concentrations and microbiome composition in the red-tide causing dinoflagellate *Alexandrium minutum* during a
961   simulated marine heatwave, Biogeosciences, 16, 4377–4391, https://doi.org/10.5194/bg-16-4377-2019 , 2019.

962   Ding, J., van der A, R., Eskes, H., Dammers, E., Shephard, M., Wichink Kruit, R., Guevara, M., and Tarrason, L.:
963   Ammonia emission estimates using CrIS satellite observations over Europe, EGUsphere [preprint],
964   https://doi.org/10.5194/egusphere-2024-1073, 2024.

965   Du, H., Li, J., Wang, Z., Dao, X., Guo, S.,Wang, L., et al.: Effects of regional transport on haze in the NorthChina
966   Plain: Transport of precursors or secondary inorganic aerosols.Geophysical Research Letters,47,e2020GL087461,
967   https://doi.org/10.1029/2020GL087461 ,2020.

968   Feick, G. and Hainer, R. M.: On the Thermal Decomposition of Ammonium Nitrate. Steady-state Reaction
969   Temperatures and Reaction Rate*, J. Am. Chem. Soc.*, 76, 22, 5860–5863, https://doi.org/10.1021/ja01651a096,
970   1954.

971 Fioletov, V., McLinden, C. A., Griffin, D., Theys, N., Loyola, D. G., Hedelt, P., Krotkov, N. A., and Li, C.:
972 Anthropogenic and volcanic point source SO_2 emissions derived from TROPOMI on board Sentinel-5 Precursor:
973 first results, Atmos. Chem. Phys., 20, 5591–5607, https://doi.org/10.5194/acp-20-5591-2020 , 2020.

974 Gao, J., Wei, Y., Guoliang, S., Yu, H., Zhang, Z., Song, S., Wang, W., Liang, D. and Feng, Y.: Roles of RH,
975 aerosol pH and sources in concentrations of secondary inorganic aerosols, during different pollution periods, Atms.
976 Environ., 241, 117770, https://doi.org/10.1016/j.atmosenv.2020.117770, 2020.

977 Ge, Y., Heal, M. R., Stevenson, D. S., Wind, P., and Vieno, M.: Evaluation of global EMEP MSC-W (rv4.34)
978 WRF (v3.9.1.1) model surface concentrations and wet deposition of reactive N and S with measurements, Geosci.
979 Model Dev., 14, 7021–7046, https://doi.org/10.5194/gmd-14-7021-2021 , 2021.

980 Giorgi, F. and Chameides, W. L.: Rainout lifetimes of highly soluble aerosols and gases as inferred from
981 simulations with a general circulation model, *J. Geophys. Res.*, 91, 367–376, 1986.

982 Goldberg, D. L., Anenberg, S. C., Kerr, G. H., Mohegh, A., Lu, Z., & Streets, D. G. : TROPOMI NO2 in the
983 United States: A detailed look at the annual averages, weekly cycles, effects of temperature, and correlation with
984 surface NO2 concentrations. Earth's Future, 9, e2020EF001665. https://doi.org/10.1029/2020EF001665. 2021.

985 Gu, B., Ju, X., Chang, J., Ge, Y. and Vitousek, P. M.: Integrated reactive nitrogen budgets and future trends in
986 China, PNAS, 112 (28) 8792-8797, https://doi.org/10.1073/pnas.1510211112, 2015.

987 He, H., Liang., X.-Z. and Wuebbles, D.J. : Effects of emissions change, climate change and long-range transport
988 on regional modeling of future U.S. particulate matter pollution and speciation, Atmos. Environ., 179, 166-176,
989 https://doi.org/10.1016/j.atmosenv.2018.02.020, 2018.

990 Holland, E. A., Braswell, B. H., Lamarque, J.-F., et al.: Variations in the predicted spatial distribution of
991 atmospheric nitrogen deposition and their impact on carbon uptake by terrestrial ecosystems, J. Geophys. Res.,
992 102, 15 849–15 866, 1997.

993 Huijnen, V., Flemming, J., Chabrillat, S., Errera, Q., Christophe, Y., Blechschmidt, A.-M., Richter, A., and Eskes,
994 H.: C-IFS-CB05-BASCOE: stratospheric chemistry in the Integrated Forecasting System of ECMWF, Geosci.
995 Model Dev., 9, 3071–3091, https://doi.org/10.5194/gmd-9-3071-2016, 2016.

996 Huijnen, V., Pozzer, A., Arteta, J., Brasseur, G., Bouarar, I., Chabrillat, S., Christophe, Y., Doumbia, T.,
997 Flemming, J., Guth, J., Josse, B., Karydis, V. A., Marécal, V., and Pelletier, S.: Quantifying uncertainties due to
998 chemistry modelling – evaluation of tropospheric composition simulations in the CAMS model (cycle 43R1),
999 Geosci. Model Dev., 12, 1725–1752, https://doi.org/10.5194/gmd-12-1725-2019, 2019.

1000 Huijnen, V., Le Sager, P., Köhler, M. O., Carver, G., Rémy, S., Flemming, J., Chabrillat, S., Errera, Q., and van
1001 Noije, T.: OpenIFS/AC: atmospheric chemistry and aerosol in OpenIFS 43r3, Geosci. Model Dev., 15, 6221–6241,
1002 https://doi.org/10.5194/gmd-15-6221-2022 ,2022.

1003 Jayne, J. T., Davidovits, P., Worsnop, D. R., Zahniser, M. S., and Kolb, C. E.: Uptake of $SO_2(g)$ by Aqueous
1004 Surfaces as a Function of pH : The Effect of Chemical Reaction at the Interface, J. Phys. Chem., *J. Phys. Chem.*,
1005 94, 15, 6041–6048, https://doi.org/10.1021/j100378a076, 1990.

1006 Jiang, Z., Zhu, R., Miyazaki, K., McDonald, B. C., Klimont, Z., Zheng, B., et al. : Decadal variabilities in
1007 tropospheric nitrogen oxides over United States, Europe, and China. Journal of Geophysical Research:
1008 Atmospheres, 127, e2021JD035872. https://doi.org/10.1029/2021JD035872, 2022.

1009 Kanakidou, M., Myriokefalitakis, S., Daskalakis, N., Fanourgakis, G., Nenes, A.,Baker, A. R., K. Tsigaridis, K. and
1010 Mihalopoulos ·N.: Past, Present and Future Atmospheric Nitrogen Deposition, J. Atmos Sci., 73(5): 2039–2047,
1011 doi: 10.1175/JAS-D-15-0278.1, 2016.

1012 Liu, L., Zhang, X., Wong, A. Y. H., Xu, W., Liu, X., Li, Y., Mi, H., Lu, X., Zhao, L., Wang, Z., Wu, X., and Wei,
1013 J.: Estimating global surface ammonia concentrations inferred from satellite retrievals, Atmos. Chem. Phys., 19,
1014 12051–12066, https://doi.org/10.5194/acp-19-12051-2019, 2019.

1015 Liu, S., Valks, P., Pinardi, G., Xu, J., Chan, K. L., Argyrouli, A., Lutz, R., Beirle, S., Khorsandi, E., Baier, F.,
1016 Huijnen, V., Bais, A., Donner, S., Dörner, S., Gratsea, M., Hendrick, F., Karagkiozidis, D., Lange, K., Piters, A.
1017 J. M., Remmers, J., Richter, A., Van Roozendael, M., Wagner, T., Wenig, M., and Loyola, D. G.: An improved
1018 TROPOMI tropospheric NO$_2$ research product over Europe, Atmos. Meas. Tech., 14, 7297–7327,
1019 https://doi.org/10.5194/amt-14-7297-2021 , 2021.

1020 Liu, S., Geng, G., Xioa, Q., Zheng, Y., Cheng, J.,and Zhang, Q.: Tracking Daily Concentrations of PM2.5
1021 Chemical Composition in China since 2000, Environ. Sci. Technol., 56, 16517-16527, 2022.

1022 Luo, G., Yu, F., and Schwab, J.: Revised treatment of wet scavenging processes dramatically improves GEOS-
1023 Chem 12.0.0 simulations of surface nitric acid, nitrate, and ammonium over the United States, *Geosci. Model Dev.*,
1024 12, 3439–3447, https://doi.org/10.5194/gmd-12-3439-2019 , 2019.

1025 Metzger, S., Dentener, F., Pandis, S., and Lelieveld, J.: Gas/aerosol partitioning: 1. A computationally efficient
1026 model, J. Geophys. Res., 107, 4312, doi:10.1029/2001JD001102, 2002.

1027 Metzger, S., Mihalopoulos, N., and Lelieveld, J.: Importance of mineral cations and organics in gas-aerosol
1028 partitioning of reactive nitrogen compounds: case study based on MINOS results, Atmos. Chemistry and Physics,
1029 6, 2549–2567, https://doi.org/10.5194/acp-6-2549-2006 , 2006.

1030 Metzger, S., Steil, B., Abdelkader, M., Klingmüller, K., Xu, L., Penner, J. E., Fountoukis, C., Nenes, A., and
1031 Lelieveld, J.: Aerosol water parameterisation: a single parameter framework, Atmos. Chem. Phys., 16, 7213–7237,
1032 https://doi.org/10.5194/acp-16-7213-2016 , 2016.

1033 Metzger, S., Abdelkader, M., Steil, B., and Klingmüller, K.: Aerosol water parameterization: long-term evaluation
1034 and importance for climate studies, Atmos. Chem. Phys., 18, 16747–16774, https://doi.org/10.5194/acp-18-16747-
1035 2018, 2018.

1036 Metzger, S., Rémy, S., Williams, J. E., Huijnen, V., and Flemming, J.: A computationally efficient
1037 parameterization of aerosol, cloud and precipitation pH for application at global and regional scale
1038 (EQSAM4Clim-v12), Geosci. Model Dev., 17, 5009–5021, https://doi.org/10.5194/gmd-17-5009-2024, 2024.

1039 Myriokefalitakis, S., Bergas-Massó, E., Gonçalves-Ageitos, M., Pérez García-Pando, C., van Noije, T., Le Sager,
1040 P., Ito, A., Athanasopoulou, E., Nenes, A., Kanakidou, M., Krol, M. C., and Gerasopoulos, E.: Multiphase
1041 processes in the EC-Earth model and their relevance to the atmospheric oxalate, sulfate, and iron cycles, Geosci.
1042 Model Dev., 15, 3079–3120, https://doi.org/10.5194/gmd-15-3079-2022, 2022.

1043
1044 Pan, D., Mauzerall, D.L., Wang, R., Guo, X., Puchalski, M., Guo, Y., Song, S., Tong, D., Sullivan, A. P., Schichtel,
1045 B. A., Collet Jr, J. L. and Zondlo, M. A.: Regime shift in secondary inorganic aerosol formation and nitrogen
1046 deposition in the rural United States. Nat. Geosci. https://doi.org/10.1038/s41561-024-01455-9 , 2024.

1047
1048 Peuch, V-H., Engelen, R., Rixen, M., Dee, D., Flemming, J., Suttie, M., Ades, M., Agustí-Panareda, A., Ananasso,
1049 C., Andersson, E., Armstrong, D., Barré, J., Nicolas Bousserez, N., Dominguez, J. J., Garrigues, S., Inness, A.,
1050 Jones, L., Kipling, Z., Letertre-Danczak, J., Parrington, M., Razinger, M., Ribas, R., Vermoote, S., Yang, X.,
1051 Simmons, A., Garcés de Marcilla, J., and Thépaut, J.-N. : The Copernicus Atmosphere Monitoring Service: From
1052 Research to Operations, BAMS, E2650–E2668, https://doi.org/10.1175/BAMS-D-21-0314.1 , 2024.

1053
1054 Reay, D. S., Dentener, F., Smith, P., Grace, J., and Feely, R. A.: Global nitrogen deposition and carbon sinks, Nat.
1055 Geosci., 1, 430–437, 2008.

1056 Rémy, S., Kipling, Z., Huijnen, V., Flemming, J., Nabat, P., Michou, M., Ades, M., Engelen, R., and Peuch, V.-
1057 H.: Description and evaluation of the tropospheric aerosol scheme in the Integrated Forecasting System (IFS-AER,
1058 cycle 47R1) of ECMWF, Geosci. Model Dev., 15, 4881–4912, https://doi.org/10.5194/gmd-15-4881-2022 , 2022.

1059 Renner, E and Wolke, R.: Modelling the formation and atmospheric transport of secondary inorganic aerosols with
1060 special attention to regions with high ammonia emissions, Atmos. Environ., 44(15),
1061 https://doi.org/10.1016/j.atmosenv.2010.02.018, 2010.

1062 Rémy, S., Metzger, S., Huijnen, V, Williams, J. E. and Flemming, J.: Representation and impact of aerosol acidity
1063 in the ECMWF IFS-COMPO cycle 49R1 through the integration of EQSAM4Climv12, *Geosci. Model Dev.*,
1064 https://doi.org/10.5194/egusphere-2023-3072, 2024.

1065 Seinfeld, J. and Pandis, S.: Atmospheric Chemistry and Physics: From Air Pollution to Climate Change - second
1066 edition, New Jersey: John Wiley and Sons, 2006.

1067 Shah, V., Jacob, D. J., Moch, J. M., Wang, X., and Zhai, S.: Global modeling of cloud water acidity, precipitation
1068 acidity, and acid inputs to ecosystems, *Atmos. Chem. Phys.*, 20, 12 223–12 245, https://doi.org/10.5194/acp-20-
1069 12223-2020, 2020.

1070 Sharma, S. K., Singh, A. K., Saud, T., Mandal, T. K., Saxena, M., Singh, S., Ghosh, S. K., and Raha, S.:
1071 Measurement of ambient NH_3 over Bay of Bengal during W_ICARB Campaign, *Ann. Geophys.*, 30, 371–377,
1072 https://doi.org/10.5194/angeo-30-371-2012 , 2012.

1073 Sharma, S., Chandra, M. and Kota, S.H.: Health Effects Associated with $PM_{2.5}$: a Systematic Review, *Curr*
1074 *Pollution Rep* **6**, 345–367, https://doi.org/10.1007/s40726-020-00155-3, 2020.

1075 Shephard, M. W., Cady-Pereira, K. E., Luo, M., Henze, D. K., Pinder, R. W., Walker, J. T., Rinsland, C. P., Bash,
1076 J. O., Zhu, L., Payne, V. H., and Clarisse, L.: TES ammonia retrieval strategy and global observations of the spatial
1077 and seasonal variability of ammonia, Atmos. Chem. Phys., 11, 10743–10763, https://doi.org/10.5194/acp-11-
1078 10743-2011, 2011.

1079 Shi, G., Xu, J., Shi, X., Liu, B., Bi, X.,Xiao, Z., et al: Aerosol pH dynamics during haze periods in an urban
1080 environment in China: Use of detailed, hourly, speciated observations to study the role of ammonia availability
1081 and secondary aerosol formation and urban environment.Journal of Geophysical Research:Atmospheres,124,
1082 9730–9742. https://doi.org/10.1029/2018JD029976, 2019.

1083 Sindelarova, K., Markova, J., Simpson, D., Huszar, P., Karlicky, J., Darras, S., and Granier, C.: High-resolution
1084 biogenic global emission inventory for the time period 2000–2019 for air quality modelling, Earth Syst. Sci. Data,
1085 14, 251–270, https://doi.org/10.5194/essd-14-251-2022 , 2022.

1086 Simpson, D, Aas, W., Bartnicki, J., Berge, H., Bleeker, A., Cuvelier, C., Dentener, F., Dore, A. Erisman, J.-W.,
1087 Fagerli, H., Flechard, C., Hertel, O., Jaarsveld, H., Jenkin, M.E., Schaap, M. Smeena, V.S., Thunis, P., Vautard,
1088 R. and Vieno, M.: Atmospheric transport and deposition of reactive nitrogen in Europe. The European Nitrogen
1089 Assessment, 298-316, doi:10.1017/CBO9780511976988.017, 2010.

1090 Simpson, R. M. C., S. G. Howell,B. W. Blomquist, A. D. Clarke, and B. J.Huebert, Dimethyl sulfide:
1091 Lessimportant than long-range transport as a source of sulfate to the remote tropical Pacific marine boundary
1092 layer,J. Geophys. Res. Atmos., 119, 9142–9167, doi:10.1002/2014JD021643 , 2014.

1093 Soulie, A., Granier, C., Darras, S., Zilbermann, N., Doumbia, T., Guevara, M., Jalkanen, J.-P., Keita, S., Liousse,
1094 C., Crippa, M., Guizzardi, D., Hoesly, R., and Smith, S.: Global Anthropogenic Emissions (CAMS-GLOB-ANT)
1095 for the Copernicus Atmosphere Monitoring Service Simulations of Air Quality Forecasts and Reanalyses, Earth
1096 Syst. Sci. Data Discuss. [preprint], https://doi.org/10.5194/essd-2023-306 , in review, 2023.

1097 Sun, Y. , Guo, G., Li, Y., Luo, G., Li, L., Yuan, H., Mur, L. A. J. and Guo, S.: Negative effects of the simulated
1098 nitrogen deposition on plant phenolic metabolism: A meta-analysis, *Sci. Total Environ.,* 19, 137–142, 2020.

1099 Tan, J., Fu, J. S., Dentener, F., Sun, J., Emmons, L., Tilmes, S., Sudo, K., Flemming, J., Jonson, J. E., Gravel, S.,
1100 Bian, H., Davila, Y., Henze, D. K., Lund, M. T., Kucsera, T., Takemura, T., and Keating, T.: Multi-model study
1101 of HTAP II on sulphur and nitrogen deposition, *Atmos. Chem. Phys.*, 18, 6847–6866, https://doi.org/10.5194/acp-
1102 18-6847-2018 , 2018.

1103 Tichý, O., Eckhardt, S., Balkanski, Y., Hauglustaine, D., and Evangeliou, N.: Decreasing trends of ammonia
1104 emissions over Europe seen from remote sensing and inverse modelling, Atmos. Chem. Phys., 23, 15235–15252,
1105 https://doi.org/10.5194/acp-23-15235-2023, 2023.

1106 Tørseth, K., Aas, W., Breivik, K., Fjæraa, A. M., Fiebig, M., Hjellbrekke, A. G., Lund Myhre, C., Solberg, S., and
1107 Yttri, K. E.: Introduction to the European Monitoring and Evaluation Programme (EMEP) and observed
1108 atmospheric composition change during 1972–2009, Atmos. Chem. Phys., 12, 5447–5481,
1109 https://doi.org/10.5194/acp-12-5447-2012, 2012.

1110 Turnock, S. T., Mann, G. W.,Woodhouse, M. T., Dalvi, M.,O'Connor, F. M., Carslaw, K. S., and Spracklen, D.
1111 V.: The impact of changes in cloud water pH on aerosol radiative forcing, Geophys. Res. Lett., 46, 4039–4048.
1112 https://doi.org/10.1029/2019GL082067, 2019.

1113 Ting. Y.C., Young, L.H., Lin TH, Tsay, S.C., Chang, K.E. and Hsiao, T.C: Quantifying the impacts of $PM_{2.5}$
1114 constituents and relative humidity on visibility impairment in a suburban area of eastern Asia using long-term in-
1115 situ measurements. Sci Total Environ. 2022 Apr 20;818:151759. doi: 10.1016/j.scitotenv.2021.151759. Epub 2021
1116 Nov 22. PMID: 34822889, 2022.

1117 Tørseth, K., Aas, W., Breivik, K., Fjaeraa, A. M., Fiebig, M., Hjellbrekke, A. G., Lund-Myrhe, C., Solberg, S. and
1118 Yttri, K. E.: Introduction to the European Monitoring and Evaluation Programme (EMEP) and observed
1119 atmospheric composition change during 1972–2009, Atmos. Chem. Phys., 12, pp. 5447-5481, 2012.

1120 van Noije, T. P. C., Le Sager, P., Segers, A. J., van Velthoven, P. F. J., Krol, M. C., Hazeleger, W., Williams, A.
1121 G., and Chambers, S. D.: Simulation of tropospheric chemistry and aerosols with the climate model EC-Earth,
1122 Geosci. Model Dev., 7, 2435–2475, https://doi.org/10.5194/gmd-7-2435-2014, 2014.

1123 Verheggen, B., Cozic, J., Weingartner, E., Bower, K., Mertes, S., Connolly, P., Gallagher, M., Flynn, M.,
1124 Choularton, T., and Baltensperger, U.: Aerosol partitioning between the interstitial and the condensed phase in
1125 mixed-phase clouds, Journal of Geophysical Research: Atmospheres, 112,
1126 https://doi.org/https://doi.org/10.1029/2007JD008714, 2007.

1127 Willem W. Verstraeten, W. W., Klaas Folkert Boersma, K. F. , Douros, J., Williams, J. E., Eskes, H., Liu, F.,
1128 Beirle, S. and Delcloo, A.: Top-Down NOX Emissions of European Cities Based on the Downwind Plume of
1129 Modelled and Space-Borne Tropospheric NO2 Columns, Sensors, 18, 2893, http://dx.doi.org/10.3390/s18092893,
1130 2018.

1131 Vestreng, V., Myhre, G., Fagerli, H., Reis, S., and Tarrasón, L.: Twenty-five years of continuous sulphur dioxide
1132 emission reduction in Europe, Atmos. Chem. Phys., 7, 3663–3681, https://doi.org/10.5194/acp-7-3663-2007,
1133 2007.

1134 Vieno, M., Heal, M. R., Hallsworth, S., Famulari, D., Doherty, R. M., Dore, A. J., Tang, Y. S., Braban, C. F.,
1135 Leaver, D., Sutton, M. A., and Reis, S.: The role of long-range transport and domestic emissions in determining
1136 atmospheric secondary inorganic particle concentrations across the UK, Atmos. Chem. Phys., 14, 8435–8447,
1137 https://doi.org/10.5194/acp-14-8435-2014 , 2014.

1138 Wang, J., Xu, J., He, Y., Chen, Y., and Meng, F.: Long range transport of nitrate in the low atmosphere over
1139 Northeast Asia, Atmos. Environ., 144, 315-324, https://doi.org/10.1016/j.atmosenv.2016.08.084, 2016.

1140 Wang, R., Guo, X., Pan, D., Kelly, J. T., Bash, J. O., Sun, K., Paulot, F., Clarisse, L., Van Damme, M., Whitburn,
1141 S., Coheur, P-F., Clerbaux, C. and Zondlo, M. A.: Monthly patterns of ammonia over the contiguous United States
1142 at 2-km resolution. Geophysical Research Letters, 48, e2020GL090579. https://doi.org/10.1029/2020GL090579

1143 Williams., J. E., van der Swaluw, E., de Vries, W. J., Sauter, F. J., van Pul, W.A.J. and Hoogerbrugge, R.:
1144 Modelling the future distribution of ammonium nitrate concentrations in The Netherlands for 2020: The sensitivity
1145 to meteorological parameters, Atmos. Environm., Volume: 115, 278-285, doi: 10.1016/j.atmosenv.2015.06.001,
1146 2015.

1147 Williams, J. E. ., Huijnen, V., Bouarar, I., Meziane, M., Schreurs, T., Pelletier, S., Marécal, V., Josse, B., and
1148 Flemming, J.: Regional evaluation of the performance of the global CAMS chemical modeling system over the
1149 United States (IFS cycle 47R1), Geosci. Model Dev., 15, 4657–4687, https://doi.org/10.5194/gmd-15-4657-2022 ,
1150 2022.

1151   Ye, X., Arab, P., Ahmadov, R., James, E., Grell, G. A., Pierce, B., Kumar, A., Makar, P., Chen, J., Davignon, D.,
1152   Carmichael, G. R., Ferrada, G., McQueen, J., Huang, J., Kumar, R., Emmons, L., Herron-Thorpe, F. L., Parrington,
1153   M., Engelen, R., Peuch, V.-H., da Silva, A., Soja, A., Gargulinski, E., Wiggins, E., Hair, J. W., Fenn, M., Shingler,
1154   T., Kondragunta, S., Lyapustin, A., Wang, Y., Holben, B., Giles, D. M., and Saide, P. E.: Evaluation and
1155   intercomparison of wildfire smoke forecasts from multiple modeling systems for the 2019 Williams Flats fire,
1156   Atmos. Chem. Phys., 21, 14427–14469, https://doi.org/10.5194/acp-21-14427-2021 , 2021

1157   Zhang, L., Jacob, D. J., Knipping, E. M., Kumar, N., Munger, J. W., Carouge, C. C., van Donkelaar, A., Wang, Y.
1158   X., and Chen, D.: Nitrogen deposition to the United States: distribution, sources, and processes, Atmos. Chem.
1159   Phys., 12, 4539–4554, https://doi.org/10.5194/acp-12-4539-2012, 2012.

1160

1161